Deutsches Zentrum
für Luft- und Raumfahrt

Ferdinand Elhardt

Vibration Damping for Highly Compliant Robots

Bachelor's Thesis
06. 12. 2018

Prof. Dr.-Ing. habil. Boris Lohmann
Johannes Strohm, M.Sc.
Manuel Keppler, Dipl.Ing.

Erklärung

Hiermit erkläre ich, die vorliegende Arbeit selbstständig durchgeführt zu haben und keine weiteren Hilfsmittel und Quellen als die angegebenen genutzt zu haben. Mit ihrer unbefristeten Aufbewahrung und Bereitstellung in der Lehrstuhlbibliothek erkläre ich mich einverstanden.

Garching bei München, den 06. 12 2018 _____ (Ferdinand Elhardt)

☐ Ich stelle die Software, die ich im Rahmen dieser Arbeit entwickelt habe, dem Lehrstuhl für Regelungstechnik unter den Bedingungen der 3-Klausel-BSD-Lizenz zur Verfügung. Ich behalte dabei die sämtlichen Urheber- sowie Nutzungsrechte und werde als Autorin namentlich genannt.

Garching bei München, den 06. 12 2018 _____ (Ferdinand Elhardt)

Chair of Automatic Control (Prof. Dr.-Ing. habil. Boris Lohmann)
Technical University of Munich
Boltzmannstraße 15
85748 Garching bei München
Germany

Lehrstuhl für Regelungstechnik (Prof. Dr.-Ing. habil. Boris Lohmann)
Technische Universität München
Boltzmannstraße 15
85748 Garching bei München
Deutschland

Contents

Task Description

Im Angesicht neuer Aufgabenfelder stoßen klassische, starre Roboter an ihre Limits. Um die Robustheit, Performance und auch Energieeffizienz von Robotern zu erhöhen, geht in der Robotik ein Trend hin zur Entwicklung von hochelastischen Robotersystemen. In solchen Robotern (z.B. DLR David oder CRunner) ist die Antriebsseite von der Abtriebsseite über einen elastischen Mechanismus entkoppelt. Um die intrinsischen Vorteile von nachgiebigen Robotersystemen maximal auszunutzen, werden diese oftmals so ausgelegt, dass die Dämpfung und Reibung parallel zu den Federn vernachlässigbar sind. Dadurch tritt eine teilweise unerwünschte, systeminhärente Schwingungsdynamik auf. Das Ziel dieser Arbeit ist die Untersuchung, ob Konzepte zur Schwingungstilgung aus der klassischen Mechanik auf unsere Regelungskonzepte [1],[2] für elastisch bzw. visko-elastisch aktuierte Systeme übertragen werden können. Insbesondere gilt zu überprüfen, ob die Motorträgheit mit Motor- sowie Getriebereibung zur Schwingungstilgung der Abtriebsseite ausgenutzt werden kann. Dabei hofft man auf eine gesteigerte Effizienz, da eine aktive Motordämpfung durch die mechanische Dämpfung bei Motor und Getriebe ersetzt wird. Die Funktionalität der theoretischen Konzepte soll in der Simulation analysiert werden.

Arbeitspakete

In der Bachelorarbeit geht es um die Frage, ob Konzepte der passiven Schwingungstilgung in der Regelung von serial elastic actuated (SEA) und serial viscous elastic actuated (SVEA) angewendet werden können. Für den SEA-Fall wird eine Variierbarkeit der Steifigkeit angenommen und für den SVEA-Fall eine Variierbarkeit der Steifigkeit als auch des Dämpfungsparameters.

Generelles

- Anpassung der Simulation für unseren Eingelenksprüfstand in Simulink, sowohl für die SEA als auch die SVEA Konfiguration.
- Anpassung der Simulation für den Eingelenksprüfstand

- Implementierung der Regelgesetze [2] und [3].

Zu beantwortende Fragen

Die resultierenden Dynamiken der geschlossenen Regelschleifen lassen sich jeweils als Zweimassenschwinger mit mehreren Federn und Dämpfern visualisieren.

SEA Wie effizient lässt sich das Konzept eines Schwingungstilger umsetzen, wenn der Dämpfer des Schwingungstilgers nicht zwischen Schwingungstilger und zu tilgender Masse wirkt, sondern zwischen Schwingungstilger und Umgebung?

SEA/VSEA In der Simulation gilt es zu untersuchen, ob link-seitige periodische Störungen effizienter gedämpft werden können, wenn die Motorträgheit als Schwingungstilger ausgelegt wird. Dazu ist die Definition eines geeigneten Kostenfunktionals essentiell.

Abstract

In order to guarantee save interaction of robots with the environment and to ensure mechanical robustness, one of the key technical properties of robotic systems is physical compliance of the actuation systems. This is mostly achieved by a highly elastic element decoupling the link from the motor.

The flexible elements cause a partially undesired vibration dynamics in the robotic structure when excited with harmonic torque on the link sides. The aim of this thesis is to analyze and to reduce oscillations through optimally chosen settings of the controller. To achieve that, we focus on two controll approaches, namely *Elastic Structure Preserving Impedance* (ESπ) and *Visco-Elastic Structure Preserving Impedance* (VESπ) controller developed by Keppler et al. in [Kep+18a] and [Kep+18b]. To analyze the closed-loop system, we focus on a non-tracking case, one joint and linear spring characteristic. As the aim is to absorb the introduced energy as efficiently as possible, we investigate the effect on certain tuning parameters.

The physically motivated design approach of ESπ and VESπ controllers enables us to represent the closed-loop system as a nonconservative multi-spring-damper two-mass oscillator. Taking the concept of a tuned mass damper (TMD) into account, we extend the existing rule of how to choose the impedance of the absorber presented in [Har56] for use in the VESπ and ESπ system. This is achieved in two steps: Firstly, we derive an analytical model of the closed-loop system and find parameters for the minimax amplitude in the frequency response. Secondly, we run a Monte Carlo simulation using a visco-elastic two-mass-system controlled by ESπ and VESπ. We want to obtain cost values for vibration and power efficiency that represent vibration efficiency and control effort.

The results provide a guideline to determine the parameters for either minimum amplitude at link-side or best power efficiency. One of the most interesting contributions is that the VESπ controller – in contrast to ESπ – features optimal damping characteristic for all excitation frequencies given the optimal setting. On the other hand, the control approach ESπ cannot be used as a TMD due to the placement of the damper. Nevertheless, an optimal setting for a wide range of frequencies can be found.

Kurzfassung

Um Roboter sicher mit Umgebung und Menschen interagieren zu lassen, ist eine Nachgiebigkeit des Robotersystem nötig. Damit wird sichergestellt, dass Schäden auf Umgebungs- und Roboterseite durch elastische Energieaufnahme vermieden werden.

Das elastische Element verursacht jedoch eine teilweise unerwünschte Bewegungsdynamik im Robotersystem. So ist das Ziel dieser Arbeit, diese Vibrationen zu analysieren und zu verhindern. Dazu werden zwei Reglerkonzepte untersucht: Die VESπ und ESπ Reglerkonzepte, von Manuel Keppler et al. entwickelt und in [Kep+18a] und [Kep+18b] präsentiert. In dieser Arbeit wird der Regulationsmodus mit konstanter Zielposition eingesetzt und eine externe, harmonische Momentenanregung auf Linkseite eingebracht. Es gilt, eine Parameterauslegung zu erarbeiten, mit der die eingebrachte Energie möglichst effizient absorbiert wird.

Der physikalisch orientierte Reglerentwurf ermöglicht eine Verhalten-Repräsentation des geregelten Systems durch ein nicht-konservatives Mehrmassen-Schwingungssystem. Mit dem Schwingungstilger-Konzept als Vorbild soll eine Erweiterung der Parametervorschrift entwickelt werden, die eine optimale Einstellung des VESπ und ESπ Systems ermöglicht. Dazu sind zwei Schritte nötig: Zuerst wird ein analytisches Modell des geschlossenen Regelkreises hergeleitet. Im Anschluss wird eine Monte-Carlo Simulation des visko-elastisches Mehrkörper-Schwingungssystems mit einer breiten Parametervariation absolviert. Dazu gilt es, einen geeigneten Satz von Kostenfunktionen einzuführen und im Analysevorgang zu verwenden.

Es ist hervorzuheben, dass der VESπ Regler – im Gegensatz zum ESπ Regler – mit einer optimalen Impedanz-Einstellung versehen werden kann, bei der die größte Amplitudenüberhöhung über das gesamte Frequenzspektrum minimiert wird. Dagegen weist der ESπ Regler keine Schwingungtilger-Charakteristik auf. Bei diesem lassen sich keine optimalen Parameter finden, die eine minimierte Maximalamplitudenüberhöhung sicherstellen. Trotzdem kann für gegebene Anregungsfrequenzen eine optimale Reglereinstellung gefunden werden. Zugleich wird für beide Regleransätze eine Parameterwahl für die Minimierung weiterer Kostenfunktionen, wie das maximale Motordrehmoment oder die durchschnittliche Leistungszufuhr des Motors präsentiert.

Mit den hergeleiteten Anweisungen können die oben genannten Regler optimal eingestellt werden, um eine Reduktion der Amplitudenüberhöhung und Maximierung der Leistungseffizienz zu erreichen. Frequenzabhängige Einstellungsvorschriften bieten eine Möglichkeit, bei bekannter Anregungsfrequenz das System einzustellen.

Symbols and Acronyms

0.1 Symbols

t	time	s
t_{start}	start time of one period	s
t_{end}	end time of one period	s
M	moment of inertia of link	$\mathrm{kg\,m^2}$
B	moment of inertia of motor with gear	$\mathrm{kg\,m^2}$
K	spring between inertia M and B	$\mathrm{N\,rad^{-1}}$
K_q	spring between inertia M and ground	$\mathrm{N\,rad^{-1}}$
K_η	spring between inertia B and ground	$\mathrm{N\,rad^{-1}}$
D_η	VESπ: damper between inertia M and B, ESπ: damper between ground and inertia B	$\mathrm{s\,N\,rad^{-1}}$
D_q	damper between inertia M and ground	$\mathrm{s\,N\,rad^{-1}}$
τ_m	control input	N m
$q(t)$	coordinate for rotation of inertia M	rad
q_0	amplitude of harmonic movement of coordinate q	rad
q_{stat}	$= P_0/K_q$: static deflection of coordinate q	rad
$\bar{q}$	amplitude ratio q_0/q_{stat}	-
$\bar{q}_{max}$	maximum amplitude ratio over selected range of excitation frequencies	-
$\eta(t)$	virtual coordinate for rotation of inertia B in closed-loop system	rad
η_0	amplitude of harmonic movement of coordinate η	rad
$\bar{\eta}$	amplitude ratio η_0/q_{stat}	-
$\bar{\eta}_{max}$	maximum normalized amplitude for all frequencies of coordinate η	-
$\theta(t)$	coordinate for rotation of inertia B	rad
θ_0	amplitude of coordinate θ	rad
$\bar{\theta}$	amplitude ratio θ_0/q_{stat}	-
q_d	desired position of q	rad
$\tau_m(t)$	motor torque	N m
$\tau_{m,0}$	motor torque amplitude	N m
$\bar{\tau}_m$	normalized motor torque τ_m/P_0	-

$\bar{\tau}_{m,max}$	maximum normalized motor torque	-
τ_{ext}	external torque applied on the system	$\mathrm{N\,m}$
$\tau_{coulomb}$	torque due to Coulomb friction	$\mathrm{N\,m}$
$\tau_{viscose}$	torque due to viscose friction	$\mathrm{N\,m}$
τ_{fric}	torque due to friction	$\mathrm{N\,m}$
τ_{joint}	torque at one joint	$\mathrm{N\,m}$
$P(t)$	torque of forced vibration	$\mathrm{N\,m}$
P_0	amplitude of forced vibration	$\mathrm{N\,m}$
ω	frequency of forced vibration	$\mathrm{rad\,s^{-1}}$
$P_{M,mean}$	average power of motor over one period	$\mathrm{W\,N^{-1}\,m^{-1}}$
$P_{br,mean}$	average breaking power of motor over one period	$\mathrm{W\,N^{-1}\,m^{-1}}$
$P_{mech,mean}$	average mechanical power over one period	$\mathrm{W\,N^{-1}\,m^{-1}}$
$P_{ext,mean}$	average external power over one period	$\mathrm{W\,N^{-1}\,m^{-1}}$
$P_{norm,1}$	normalized power consumption of the motor	$\mathrm{W\,N^{-1}\,m^{-1}}$
μ	$= B/M$: inertia ratio	-
$\omega_{\eta,n}^2$	$= K/B$: natural frequency of inertia B	-
$\omega_{q,n}^2$	$= K_q/M$: natural frequency of inertia M	-
f	$= \omega_{\eta,n}/\omega_{q,n}$: frequency ratio of natural frequencies	-
g	$= \omega/\omega_{q,n}$: excitation frequency ratio	-
q_{stat}	$= P_0/K_q$: static deflection of system	rad
ξ_q	$= \frac{D_q}{2M\omega_{q,n}}$: damping ratio of inertia M	-
ξ_η	$= \frac{D}{2B\omega_{\eta,n}}$: damping ratio of inertia B (for VESπ)	-
ξ_η	$= \frac{D_\eta}{2B\omega_{\eta,n}}$: damping ratio of inertia B (for ESπ)	-

0.2 Abbreviations and acronyms

TMD tuned mass damper ix

SEA series elastic actuator vi

VSEA viscous series elastic actuator vi

DLR Deutsches Zentrum für Luft- und Raumfahrt 1

MIT Massachusetts Institute of Technology 6

Chapter 1

Introduction

In the development of traditional robots, it is desirable to increase the structure's stiffness as much as possible to ensure best positioning performance, stability and bandwidth of position-control. Even strong acceleration and heavy loads should not lead to deflection of the structure. A lot of effort is made to reduce elasticity in all components, including structure, gear and bearing. This endeavor is paying of: In many cases elasticity is negligible and the system is primarily dominated by the rigid body part which greatly reduces effort in control.

Despite of the many advantages of rigid actuators, a lack of elasticity comes with a great drawback. Most electric motors have limited torque abilities which means that they can provide high power density only at high speed. This leads to the necessity of gear reduction to be able to accelerate loads like a robot link. Unfortunately, gear reduction increases the reflected inertia of the motor which causes much higher shock loads on the teeth of the gear system in case of a collision.

In order to make a robot more robust against impacts and unknown contact forces, researchers have developed and presented physical compliant robots as a new possibility in [PW95] to gain new objectives. This reduces shock forces on mechanical parts like motor and gear. Robots with a series elastic actuator (SEA) or a viscous series elastic actuator (VSEA) have a highly elastic element in the drive train, either with (VSEA) or without (SEA) a damping element which is able to absorb a large portion of the collision energy. Moreover, compliance in robots increases safety towards human interaction. This has been studied using a pneumatic arm in [Dam+07] and the *David system* (earlier: Hand/Arm System) developed by Deutsches Zentrum für Luft- und Raumfahrt (DLR) and presented in [Gre+11] where physical compliance was reached by installing a spring between motor and link. Moreover elastic elements act like an energy storage that can be exploited. This is useful for cycling tasks like hammering, drumming, or locomotion. That mechanical energy storage is an advantage for the process of walking

was demonstrated with the foot prosthesis in [Che+12]. It compresses a spring and releases it in every step to increase power efficiency. In addition, elastic elements support the dynamics for explosive movements. Jumping or throwing sometimes makes it necessary to go beyond the natural motor's capabilities. Since the motor's energy and the elastic element's force accumulate, motions can be faster and more powerful. As an economic factor, it should be noted that the elastic element replaces an expensive and fragile torque sensor, as the torque can be simply measured using its deflection.

However, physical compliance comes with a huge drawback as it requires complex control algorithms and well-advanced sensor systems to achieve a well controlled system. This is necessary due to intrinsic oscillatory dynamics of the two-mass-system. Moreover, the number of dimensions of the configuration space is double the number of dimension of the control input space: A rigid robot system with one joint has one degree of freedom since the link is directly connected to gear and motor. A compliant robot system with one joint has two degrees of freedom. One is described as the motor coordinate and the other as the link coordinate. Both positions can be moved but in contrast to the motor coordinate the compliant coordinate cannot be actuated directly. This leads to an under-actuated system.

In DLR, control approaches namely VESπ and ESπ for compliantly actuated robots have been developed and proposed in [Kep+18b] and [Kep+18a]. They allow to define a manner of the robot's interaction with its environment. The physically motivated design approach of ESπ and VESπ controllers allows to completely represent the closed-loop behavior of the controller as a nonconservative multi-spring-damper system. This provides a physically intuitive interpretation that only consists of inertias, springs and dampers.

While some parameters are defined by the preservation of the hardware's characteristic – like inertia of link, inertia of motor and impedance of internal elastic element – others are free to determine. On the one hand, there are parameters considered to be changed by the user in terms of specifying the links dynamics. On the other hand, there are some parameters that influence the system in a less intuitive way which makes it hard to choose the best fitting values.

This work deals with the analysis and tuning of the controller to give an well-founded advice how to choose these parameters. Tuning can only be successfully done with respect to a certain, well defined task. That is why this work only considers the behavior of a SEA and VSEA controlled by the ESπ and VESπ controllers without tracking. This means, the desired position of the link is constant for the whole experiment. To disturb the system, we excite it with an external harmonic torque at link side. This task is relevant when a robot is walking and a harmonic torque is applied to the arms which start swinging. The question is, how the system behaves when excited with a harmonic torque. Does it overshoot? How much energy

is needed to damp the movement? How can the parameters be changed for stiffness and damping to make the system reducing certain cost values?

To answer these questions, a study is made on how the parameters influence the system dynamics and the control cost. First, the concept of a TMD is taken as an example to study the effect of a damper in a two mass system. As it is a well developed theory with guidelines for tuning the parameters in terms of a reduction of the link's amplitude, research is done to find parallels.

For transferring the knowledge about a TMD to VESπ and ESπ system, a few fundamental differences should be considered. First, springs and dampers are connected at different places. A TMD has one spring between main mass and environment as it can be seen in Figure 1.1. In the closed-loop system of the VESπ controller (Figure 1.2), there is an additional damper in between the two masses. In the ESπ system (Figure 1.2), there is a additional damper connected to the environment. Secondly, the concepts differ at the choice of the mass ratio. According to [IRS08], the TMD in Taiwanese *TAIPEI 101* weights 660 t while the building itself weights 700.000 t. This gives a ratio of about 1/100. Other TMD feature a mass ratio of 1/20. In contrast to that, typical robot system feature a mass ratio of more than 2 which means that the link inertia is only half of the motor inertia. This causes a fundamental different behavior which has to be studied.

First, the idea of the TMD's parameter tuning is followed and an analytical model of the closed-loop system of the VESπ and ESπ controllers are derived. This is already done for the classical TMD documented in [Har56], where optimal parameters are found for the minimum amplitude for the entire frequency space. Transferring that concept on the VESπ and ESπ controllers, it has to be recalled that the closed-loop system is not a mechanical mass system but only a theoretical construction of the closed-loop behavior. At this resulting closed-loop system, similarities can be found to the TMD and the concept can be adopted. Secondly, a simulation of a mechanical two mass system VSEA or SEA is developed, which is controlled by the ESπ or VESπ controller to run a parameter analysis with a set of parameters to obtain physically results. They include a cost value for power efficiency and coordinates for the movement of the motor.

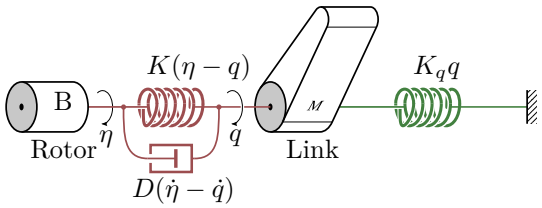

Figure 1.1: Classical TMD (Figure from [Kep+18b])

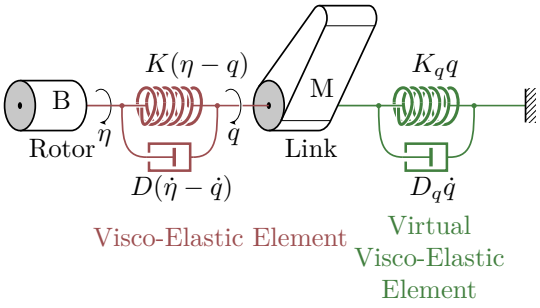

Figure 1.2: Closed-loop behavior of VESπ system (Figure from [Kep+18b])

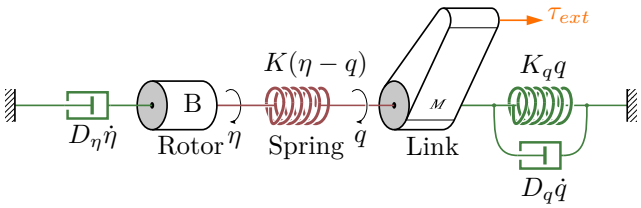

Figure 1.3: Closed-loop behavior of ESπ system (Figure from [Kep+18a])

Chapter 2

State of the Art

The idea of a TMD was initially described by DenHartog in [Har56]. From then on, the TMD system is widely used in many applications and was well developed. Using the idea of a TMD, tuning rule should be found for a compliant robot drive. As one of the first approaches Mark W. Spong described a compliant robot drive [Spo87] in 1987. Later on, a lot of investigation was done to extend and to fully understand the idea of having a flexible element in a robot system. One of the most challenging task was to create a reliable control approach for such a system. Manuel Keppler from DLR (German Aerospace Center) developed a novel approach that allows – with limitations – a torque interface at link side in his papers [Kep+18b] and [Kep+18a].

In order to find the best tuned parameters in a VESπ and ESπ system, this work exploits the well investigated concept of a TMD. Its tuning is already described in [Har56]. Design rules and optimal parameters for VESπ and ESπ controllers are developed for minimizing the amplitude when excited with a harmonic torque at link side. Moreover, we extend the approach to an optimized parameter choice in terms of power efficiency.

2.1 Tuned Mass Damper in Literature

A TMD is a multi mass-spring-damper-system that is mounted on a structure to reduce the amplitude of mechanical vibrations. Due to the simple structure a TMD is very common in power transmission, automobiles and buildings. A classical TMD is shown in Figure 2.1. The stiffness K_q forms the connection of the main mass M to its environment. This part is the natural structure, for example an automotive engine, connected to the chassis. The idea is that the additional mass B is connected to the main mass M with optimal parameters for stiffness K and damping D_η so that the main mode of the main mass M is moved to non critical frequencies or its amplitude is lowered. The resulting frequency response of main mass M is featured by two new modes that are replacing the old system's main mode.

Both modes have a lower amplitude than the old main mode. The combination of stiffness K and damping D leads a flattening of the two new modes. This can be seen in Figure 2.2.

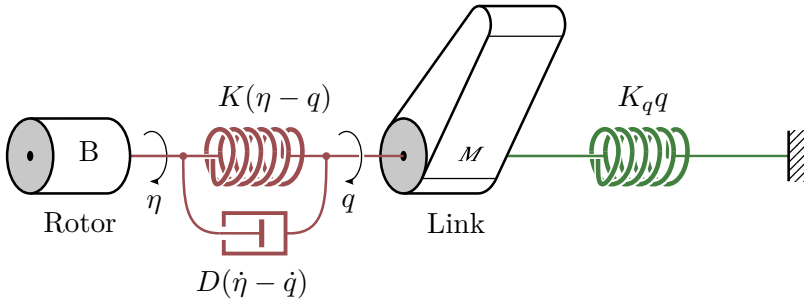

Figure 2.1: Classical TMD: The rotor mass B is mounted on link mass M with stiffness K and damping D_η. This mechanical construction reduces the vibration of coordinate q due to the mass-spring-damper-structure of B. The worst-case vibration is less intense than without it. Stiffness K and damping D_η are set dependent on the inertias M, B, and stiffness K_q. (Figure from [Kep+18b])

The Dutch/American mechanical engineer and Professor of Mechanical Engineering at Massachusetts Institute of Technology (MIT) Jacob Pieter Den Hartog found a way to determine the optimal parameters for a standard TMD. Using the system in Figure 2.1, he defined an analytic way to describe a two mass system subjected with a harmonic torque at the main mass. With the idea of a TMD in mind, that reduces the vibration's amplitude, he found an analytical equation that provides the optimal parameters for the stiffness and damping of the visco-elastic element between M and B. He described the solution in his work [Har56, page 119ff] published in 1956. In this work, complex numbers are underlined.

2.1.1 Derivation of the Oscillation Amplitude for a Tuned Mass Damper (TMD)

The equations of motion for the system 2.1 excited by the external torque $P(t)$ can be expressed as

$$\begin{aligned} B\ddot{\eta} + K(\eta - q) + D_\eta(\dot{\eta} - \dot{q}) &= 0 \\ M\ddot{q} + K_q q + K(q - \eta) + D_\eta(\dot{q} - \dot{\eta}) &= P(t)\ . \end{aligned} \tag{2.1}$$

We are only interested in the forced vibration and not in the transient free vibration. Then, q is a harmonic motion which can be represented by vectors. The frequency ω is the frequency of the excitation torque. We follow

[Har56, page 63] using the complex approach

$$\begin{aligned} x(t) &= \underline{x_0}\, e^{j\omega t} \ , \\ \dot{x}(t) &= \underline{x_0}\, j\omega e^{j\omega t} \ , \\ \ddot{x}(t) &= -\underline{x_0}\, \omega^2 e^{j\omega t} \end{aligned} \tag{2.2}$$

where

$$\begin{aligned} x(t) &= \begin{bmatrix} \eta(t) \\ q(t) \end{bmatrix} \\ \underline{x}_0 &= \begin{bmatrix} \underline{\eta}_0 \\ \underline{q}_0 \end{bmatrix} \\ \underline{x}_0 &\in \mathbb{C}^2 \end{aligned} \tag{2.3}$$

and an harmonic excitation

$$P(t) = P_0 \cdot e^{j\omega t} \tag{2.4}$$

to find a solution of these equations. The variables $\underline{\eta_0}$ and $\underline{q_0}$ express the amplitude of the harmonic excitation. We can transform the equations of motions in matrix form to

$$\begin{aligned} -\omega^2 \begin{bmatrix} B & 0 \\ 0 & M \end{bmatrix} \begin{bmatrix} \underline{\eta_0} \\ \underline{q_0} \end{bmatrix} + j\omega \begin{bmatrix} D_\eta & -D_\eta \\ -D_\eta & D_\eta \end{bmatrix} \begin{bmatrix} \underline{\eta_0} \\ \underline{q_0} \end{bmatrix} + \\ \begin{bmatrix} K & -K \\ -K & K + K_q \end{bmatrix} \begin{bmatrix} \underline{\eta_0} \\ \underline{q_0} \end{bmatrix} = \begin{bmatrix} 0 \\ P_0 \end{bmatrix} \ . \end{aligned} \tag{2.5}$$

We are primarily interested in the movement of q which is the link's rotation. We split the matrix expression (2.5) into two scalar equations and solve the one for q and the other one for η. Substituting $\underline{\eta}_0$ in the first line of (2.5) leads to an analytical expression of $\underline{q}_0$. According to [Har56, equation 54], this gives

$$\begin{aligned} \frac{\underline{q_0}}{P_0} &= \frac{A_{eq} + jB_{eq}}{C_{eq} + jD_{eq}} \\ A_{eq} &= K - B\omega^2 \\ B_{eq} &= \omega D_\eta \\ C_{eq} &= (-M\omega^2 + K_q)(-B\omega^2 + K) - B\omega^2 K \\ D_{eq} &= \omega D_\eta(-M\omega^2 + K_q - B\omega^2) \ . \end{aligned} \tag{2.6}$$

As mentioned earlier, we are only interested in the amplitude of the harmonic vibration. Since $\underline{q_0}$ is complex, we consider the equation provided by [Har56, equation 54a] to get the amplitude q_0 of the harmonic vibration. We come

to (2.7) using the Pythagorean theorem. This formula can be used for any complex equation in the form of (2.6). This yields an equation that finally provides the amplitude of the harmonic vibration of coordinate q:

$$\frac{q_0}{P_0} = \sqrt{\frac{A_{eq}^2 + B_{eq}^2}{C_{eq}^2 + D_{eq}^2}} \ . \tag{2.7}$$

In 2.7, the number of variables can be reduced. For example, if we double the amplitude P_0 of the external torque – assuming everything else stays the same – the amplitude q_0 of coordinate q will double, too. That means, we have variables that are dependent on other variables. In order to reduce the number of variables in our equation and to remove the units, we consider the definitions of the symbols introduced in chapter *Symbols*. We change (2.7) to

$$\boxed{\bar{q} = \sqrt{\frac{(2\xi_\eta g)^2 + (g^2 - f^2)^2}{(2\xi_\eta g)^2 (g^2 - 1 + \mu g^2)^2 + (\mu f^2 g^2 - (g^2 - 1)(g^2 - f^2))^2}} \ .} \tag{2.8}$$

This formula provides the amplitude ratio $\bar{q}$ of system (2.1) which is excited at coordinate η with a harmonic torque using amplitude P_0 and excitation frequency ω. According to chapter *Symbols*, $\bar{q} = q_0/q_{stat}$ is the normalized deflection, ξ_η is the damping ratio of mass B, g is the frequency ratio of the excitation torque and f is the natural frequency ratio of masses B and M. The variable μ is the inertia ratio.

It should be noted that the frequency of the link position q in (2.1) is the same as the external excitation frequency as (2.1) is a linear system.

2.1.2 Analysis of a Tuned Mass Damper (TMD)

For analytic reasons, it is important investigate the behavior for very low and very high frequencies. First, we let $g \to 0$ in (2.8). In other words, we excite the system with a given torque which should result in the static deflection for $t \to \infty$. We expect $\bar{q}$ to be 1 in

$$\bar{q} = \lim_{g \to 0} \sqrt{\frac{(2\xi_\eta g)^2 + (g^2 - f^2)^2}{(2\xi_\eta g)^2 (g^2 - 1 + \mu g^2)^2 + (\mu f^2 g^2 - (g^2 - 1)(g^2 - f^2))^2}} = \sqrt{\frac{(-f^2)^2}{((-1)(-f^2))^2}} = \frac{f^2}{f^2} = 1 \ . \tag{2.9}$$

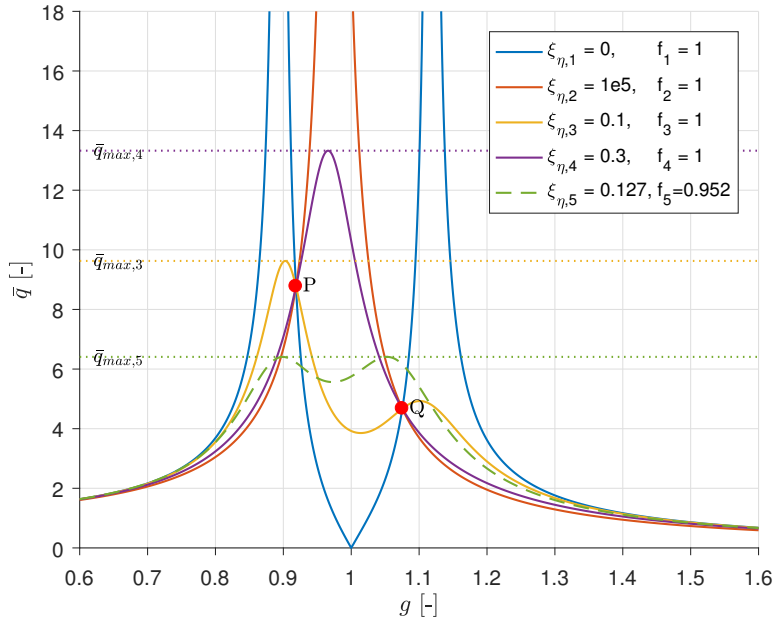

Figure 2.2: The graph shows the *amplitude ratio* $\bar{q}$ of the classical TMD when excited with the *excitation frequency ratio* g. With different *damping ratios* ξ_η, the frequency response changes fundamentally. For us, the *maximum amplitude ratio* $\bar{q}_{max}$ over the selected range of g is the most important result. This is why we labeled the *maximum amplitude ratio* for each setting of ξ_η as $\bar{q}_{max,1\ldots5}$. Additionally, at two intersection points Q and P all graphs with same value in f intersect. For this analysis, we used the mass ratio $\mu = 1/20$.

Second we let $g \to \infty$. This case can be described as an infinite high frequency of the excitation torque. We expect a result of $\bar{q} = 0$ for $g \to \infty$: Moving a mass with a infinite frequency in a infinite inertia torque prevent the inertias to move. The following equation

$$\bar{q} = \lim_{g\to\infty} \sqrt{\frac{(2\xi_\eta g)^2 + (g^2 - f^2)^2}{(2\xi_\eta g)^2 (g^2 - 1 + \mu g^2)^2 + (\mu f^2 g^2 - (g^2 - 1)(g^2 - f^2))^2}} = 0 \tag{2.10}$$

proves this assumption.

Next, we are interested in how DenHartog's TMD behaves when using different damping ratios ξ_η. We choose several different damping ratios to illustrate the differences between its behavior. Figure 2.2 shows the amplitude ratio $\bar{q}$ with several sets of *natural frequency ratio* f and *damping ratio* ξ_η. The inertia ratio μ is set to 1/20. Case $\xi_\eta = 0$ is similar to a two-mass system without any damping and features two resonant frequencies. It is obvious when $\xi = 1e5$ that the two-mass system behaves like a one-mass system. Due to the highly damped between mass B and M, they tend to stick together. As a result of the effective mass $M + B$, we see the main

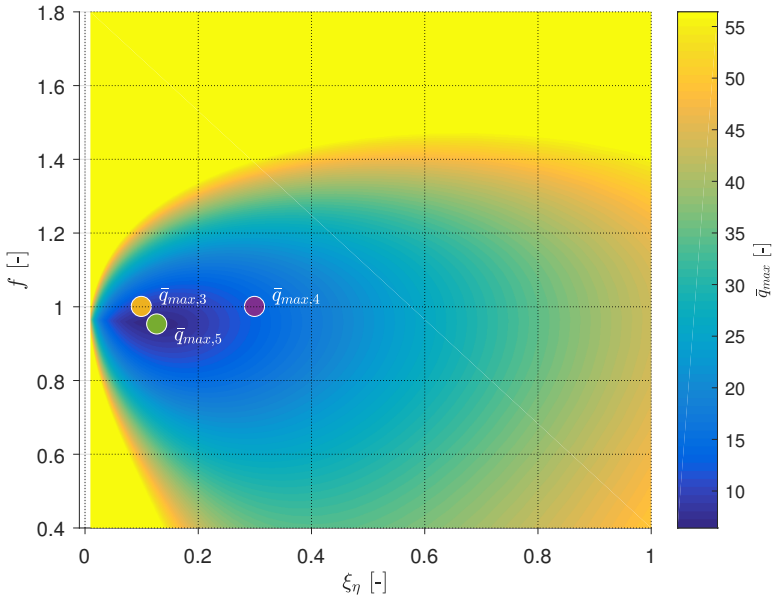

Figure 2.3: This graph shows the *maximum amplitude ratio* $\bar{q}_{max}$ of the classical TMD system. We took the values of $\bar{q}_{max,1...5}$ (Figure 2.2) and drew them in this graph at the corresponding position of the *natural frequency ratio* f and the *damping ratio* ξ_η. The color depicts the value of the *maximum amplitude ratio* $\bar{q}_{max}$. Overall, this graph shows the effect of f and ξ on $\bar{q}_{max}$. We used the mass ratio $\mu = 1/20$.

mode slightly lower than we would expect it to be with only mass M. The cases $\xi_\eta = 0.1$ and $\xi_\eta = 0.3$ illustrate two randomly chosen damping ratios. While $\xi_\eta = 0.1$ is characterized by two nicely damped main modes, $\xi_\eta = 0.3$ features only one main mode. This shows that decreasing the damping ratio leads to two main modes with high amplitudes. Increasing the damping ratio leads to one high main mode. Somewhere in the middle is an optimal value for the damping ratio so that the maximum value of the deflection is small. As we will describe later, $\xi_\eta = 0.127$ and $f = 0.952$ are the optimum values with the lowest *maximum amplitude ratio* $\bar{q}_{max}$ over the entire range of *excitation frequency ratio* g. This is shown in curve 5.

It is noticeable that all curves with the same value for f have two intersection points where all curves meet. Except of curve 5 which has a slightly different value for f. We exploit this fact for the derivation of the optimal parameters as it is described by DenHartog in [Har56].

Now, we take the *maximum amplitude ratios* $\bar{q}_{max}$ of Figure 2.2 and transfer it as a single value into a two-dimensional graph in Figure 2.3, where the axis are the *natural frequency ratio* f and the *damping ratio* ξ_η. This provides an overview of the effect of f and ξ_η on the *maximum amplitude ratio* $\bar{q}_{max}$. We can see that there is a minimum at $\xi_{opt,TMD} \approx 0.127$ and $f_{opt,TMD} \approx 0.952$ as we have already presented in Figure 2.2.

2.1.3 Optimal Parameters

We find two equations that describe the optimal setting for $f_{\text{opt, TMD}}$ on the one hand and the best damper setting $\xi_{\eta,\text{opt, TMD}}$ on the other hand. Following [Har56, eq. 63], we claim:

$$\boxed{f_{opt,\text{TMD}} = \frac{1}{1+\mu} \ .} \tag{2.11}$$

Note that the optimal setting for f is only dependent on the mass ratio μ. With the second equation (2.12) from [Har56, eq. 69, page 131], we find the optimal damping ratio

$$\boxed{(\xi_{\eta,opt,\text{TMD}})^2 = \frac{3\mu}{8(1+\mu)^3} \ .} \tag{2.12}$$

For visualizing the results, we focus on Figure 2.2. At two invariant points P and Q, all curves intersect. These points are independent of the excitation frequency ratio. In order to reduce our maximum amplitude of q, we need to find a curve that connects point P and Q with a horizontal tangent through the highest of the two fixed points.

First of all, we want these two fixed points to be on the same height. With (2.11), we achieve this claim. Second we search the horizontal tangent on one of the two points. We achieve this claim with (2.12).

2.2 VSEA and SEA as Drive Concept

In order to make robots more robust against impacts and unknown contact forces, researchers have developed physical compliant drives. Drives with SEA or VSEA have a highly elastic element in the drive train. VSEA drives have a additional damping element parallel to the elastic element. The elastic element located between motor and link inertias results in in a dynamical behavior of a low-pass filter on external influences. Shocks and collision energy are easily absorbed.

According to [PW95], series elasticity transforms the force control problem into a positioning control problem. That means that the link cannot be actuated with a commanded torque directly but only the position θ of the motor. The torque τ at link side is a result of torsion of a spring or rotation of a damper:

$$\tau = K(q-\theta) + D_\eta(\dot{q}-\dot{\theta}) \ . \tag{2.13}$$

Additionally, series elasticities are able to store energy in the springs.

2.2.1 Viscous Series Elastic Actuator (VSEA)

A VSEA drive has a highly elastic and damping element decoupling the motor coordinate θ from the link coordinate q. The basic system is shown in Figure 2.4.

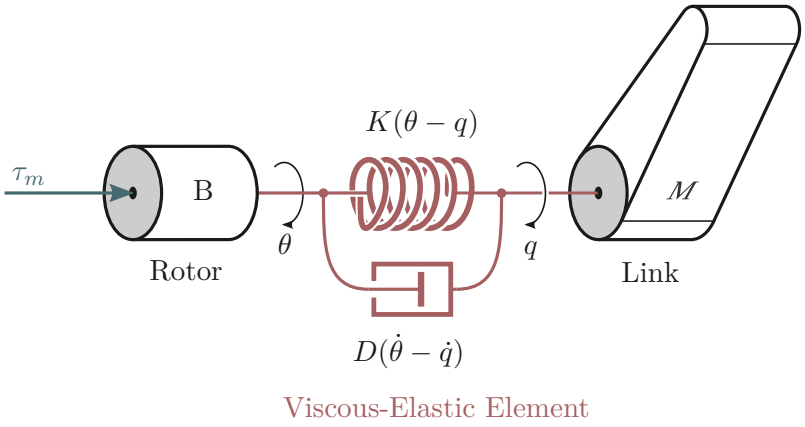

Figure 2.4: The open-loop structure of the VSEA concept consists of a spring with stiffness K and a damper with damping value D between the rotor inertia B and the link inertia M. The control input is the motor torque τ_m. (Figure from [Kep+18b])

Proposed by Spong in [Spo87], the VSEA plant dynamics with τ_m as the motor torque is described as the following:

$$\begin{aligned} M\ddot{q} &= D_\eta(\dot{\theta} - \dot{q}) + K(\theta - q) \\ B\ddot{\theta} &= D_\eta(\dot{q} - \dot{\theta}) + K(q - \theta) + \tau_m \ . \end{aligned} \tag{2.14}$$

2.2.2 Series Elastic Actuator (SEA)

A SEA drive is similar to the VSEA but without the damping element. There is only a spring between motor and link. This concept is used in the DLR *C-Runner* explained in the publication [Loe+16]. This walking robot uses linear springs in the transmission system to provide a flexible connectivity between joint and motor axis. As indicated in Figure 2.5, tendons with linear springs are used to ensure a flexible coupling between motor and joint.

The anthropomorphic robot *David* developed at DLR also uses the SEA concept in every joint. It is a platform that allows an investigation of control approaches for variable stiffness drive concepts. In contrast to many other robots, *David* can adjust its joint stiffness on-the-fly. As a drawback, the robot features nonlinear spring characteristics what makes it harder to find a simple control law. Figure 2.6 shows the basic structure of the robot. The elastic elements are integrated in the joint motors.

Figure 2.7 shows the buildup of a SEA. According to Keppler in [Kep+18a],

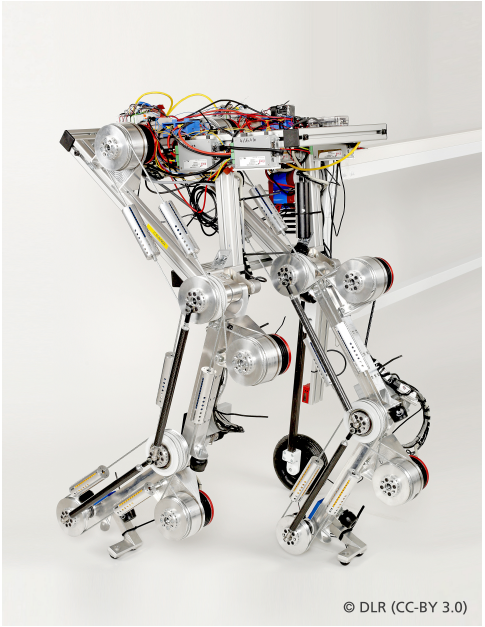

Figure 2.5: The running robot C-Runner of DLR uses the SEA drive concept in every joint, which allows tests for efficient walking. (Picture by DLR)

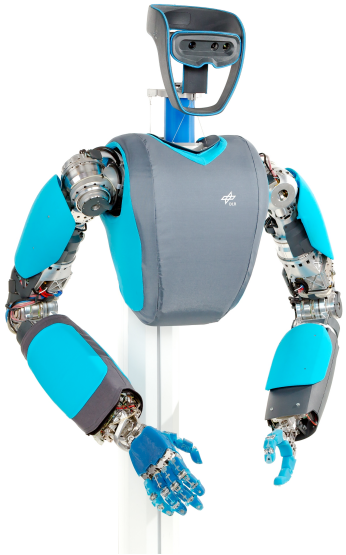

Figure 2.6: The anthropomorphic robot *David* of DLR using SEA drive concept with an adjustable stiffness and a nonlinear spring characteristic. (Picture by DLR)

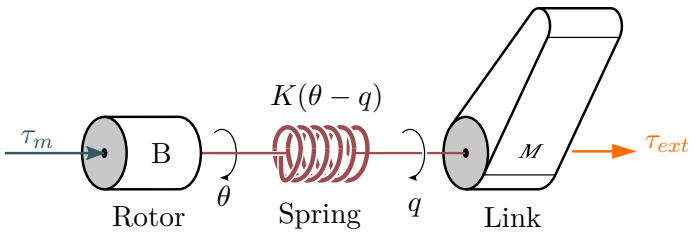

Figure 2.7: The mechanical structure of the SEA concept consists of a spring with adjustable stiffness K between the rotor inertia B and the link inertia M. The control input forms the motor torque τ_m. (Figure from [Kep+18a])

the corresponding equations are the following:

$$\begin{aligned} M\ddot{q} &= K(\theta - q) + \tau_{ext} \\ B\ddot{\theta} &= K(q - \theta) + \tau_m \ . \end{aligned} \tag{2.15}$$

2.3 Control Theory

At DLR, control approaches namely VESπ and ESπ for compliantly actuated robots have been developed and presented in [Kep+18b] and [Kep+18a]. They provide an impedance control so that the closed-loop system acts like the link was connected via spring and damper to the environment. The physically motivated design approach of ESπ and VESπ controllers allows to completely represent the closed-loop behavior of the controller as a nonconservative multi-spring-damper system. This gives us a physically intuitive interpretation in form of a mechanical substitution system that consists of inertias, springs and dampers. The parameters that describe inertias, stiffnesses and damping are sufficient to characterize the closed-loop dynamic.

2.3.1 Derivation of VESπ controller

The VESπ controller is made for using the VSEA driving joint that consists of a spring and a damper between motor and link. Controlling a VSEA with the VESπ approach leads to a behavior which can be described as the mechanical substitute system shown in Figure 2.8.

The use of the VESπ controller extends the mechanical VSEA system with an additional damper and spring at link side. As it can be seen from the graphic, we deal with two coordinates: The rotation q of the link and the position η of the virtual rotor. Note that in comparison to the mechanical system in Figure 2.4, the link coordinate q remains while the motor coordinate θ in the open-loop system changes to the virtual motor coordinate η in the closed-loop system.

The difference between the mechanical interpretation of VSEA actuated with VESπ controller and the classical TMD is an additional damper be-

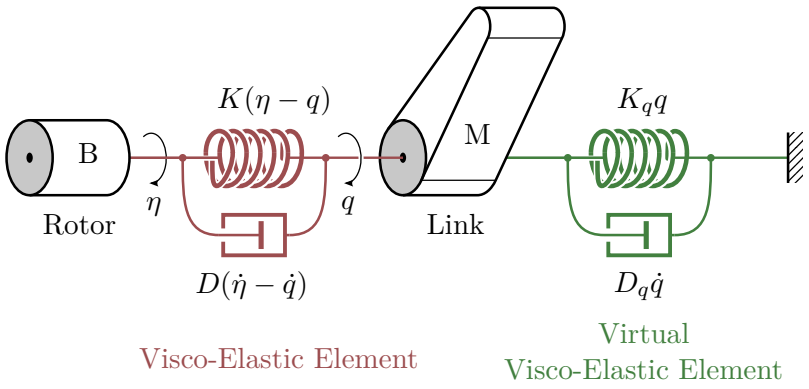

Figure 2.8: Graphical representation of the closed-loop behavior of VESπ system in terms of basic mechanical elements, such as springs, damper and inertias. The stiffness K, the damping D and the inertias (B and M) correspond with the mechanical parameters in Figure 2.4. (Figure from [Kep+18b])

tween main mass M and environment. As we want to analyze this system in a similar way as we did with the TMD in Section 2.1, this difference will play a main role later.

We want to derive the control law for this system. We need a controller that transforms the mechanical, open-loop system VSEA into the closed-loop system in Figure 2.8. We follow the explanation in [Kep+18b] for the development of the VESπ controller. We take the system dynamics of the VSEA (2.14) and choose the desired closed-loop dynamic:

$$\boxed{\begin{aligned} M\ddot{q} &= D_\eta(\dot{\eta} - \dot{q}) + K(\eta - q) - D_q\dot{q} - K_q q + \tau_{ext} \\ B\ddot{\eta} &= D_\eta(\dot{q} - \dot{\eta}) + K(q - \eta) \end{aligned}} \tag{2.16}$$

We equal (2.16) and (2.14) and come to the following coordinate transformation:

$$\dot{\theta} = \dot{\eta} - D_\eta^{-1}(D_q\dot{q} + K_q q + K(\theta - \eta) - D_\eta\dot{\eta}) \tag{2.17}$$

With the derivation of (2.17) and (2.14) and following [Kep+18b], we come to the control law for τ_m:

$$\tau_m = B\dot{a} + n \ . \tag{2.18}$$

with

$$\begin{aligned} \dot{a} &= D_\eta^{-1}(K(\dot{\eta} - \dot{\theta}) - D_q\ddot{q} - K_q\dot{q}) \\ n &= -D_q\dot{q} - K_q q \ . \end{aligned} \tag{2.19}$$

2.3.2 Derivation of ESπ controller

In this chapter, we want to derive the ESπ control approach as it is presented in the publication [Kep+18a]. This controller is made for mechanical SEA

systems that consist of a linear spring between motor and link, as shown in Subsection 2.2.2.

Controlling a SEA with the ESπ approach presented in Subsection 2.3.2 leads to a mechanical substitute system as it is illustrated in Figure 2.9. The

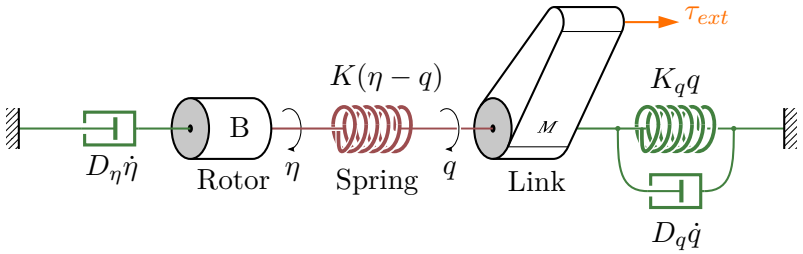

Figure 2.9: Mechanical substitute system of the closed-loop behavior of ESπ system. The values for the stiffness K and the inertias M and B correspond with the mechanical system in Figure 2.7(Figure from [Kep+18a])

ESπ controller extends the mechanical SEA plant system with an additional damper at motor side and spring and damper at link side. As we have already seen in Subsection 2.3.1, we deal with two coordinates: The rotation q of the link and the position η of the virtual rotor.

As we want to analyze this system in a similar way as we did with the TMD in Section 2.1, we have a look on how this system differs from the TMD concept. The ESπ approach changes the system fundamentally. First, there is a damper between main mass M and the environment – like we have seen with the VESπ controller. Second, we move the damper between M and B to the location between B and environment.

We follow the explanation in [Kep+18a] for the derivation of the ESπ control approach. We start with the model of a robot joint with SEA referring to (2.15) and then choose our desired closed-loop dynamic:

$$\boxed{\begin{aligned} M\ddot{q} &= K(\eta - q) - D_q\dot{q} - K_q q \\ B\ddot{\eta} &= K(q - \eta) - D_\eta\dot{\eta} \ . \end{aligned}} \tag{2.20}$$

To get the control law for τ_m, we introduce a new motor coordinate η that satisfies

$$K(\theta - q) = K(\eta - q) - \underbrace{D_q\dot{q} - K_q q}_{=:n} \ . \tag{2.21}$$

Then, we introduce the coordinate transformation

$$\theta = \eta - q - K^{-1}n + q \ . \tag{2.22}$$

For the control law, we choose

$$\tau_m = -D_\eta\dot{\eta} + BK^{-1}\ddot{n} + n \tag{2.23}$$

so that using it in (2.15) we come to (2.20).

Chapter 3

Methods

This work contributes an analysis of the influence of parameters in VESπ and ESπ controller. Inspired by the theory of the classical TMD, we defined several tuning parameters that shape the behavior of the system. One goal is to analyze the influence of these tuning parameters on link amplitude, motor torque and power consumption. We additionally want to find optimal values for the parameters to minimize these features. This chapter presents several objectives and methods.

The studies concentrate on the case when the system is excited with an external, harmonic torque τ_{ext} at the link with coordinate q. The excitation torque is defined as

$$\tau_{ext} = P_0 \, sin(t\omega). \tag{3.1}$$

Hereby, P_0 is the amplitude of the torque, ω is the excitation frequency and t is the time.

Two different methods are used for the analysis. First, we derive an analytical approach that provides the amplitude ratio of the link coordinate. This approach directly processes the closed-loop dynamics of VESπ and ESπ controller. It is easy to evaluate since it is a simple equation, but this method is limited: We cannot consider controller-internal information, like motor torque or friction. This is why we use a simulation in *Matlab Simulaink* as a second method. Here, we run a model of the open-loop system VSEA and SEA as explained in Subsection 2.2.1 and 2.2.2. The simulation of the mechanical system is controlled by the VESπ and ESπ controller to study its behavior. This approach includes friction and numerical errors due to the processing solver in *Matlab Simulink*. In return, we gain results for motor behavior, power consumption and normalized power consumption.

We take advantage of the mechanical motivated design of the control approaches VESπ and ESπ which allow us to see the closed-loop system as a mechanical oscillator. Both systems, VESπ and ESπ feature the following parameters:

- M: the inertia of the link
- B: the inertia of the motor
- K_q: the stiffness of the spring between environment and link
- K: the stiffness of the spring between the inertia M and B
- ξ_q: the damping ratio of inertia M
- ξ_η: the damping ratio of inertia B

System attributes, like inertias M and B, are mechanical parameters which cannot be changed on the fly. Nevertheless, we want to analyze several inertia ratios. This is important because with different robot configurations, the link's inertia can change. With stretched out robot arm the inertia is much higher than in bent configuration.

We follow the idea of the impedance control approach which is defined by the controlling of the dynamics interaction between a manipulator and its environment. That means, the stiffness K_q and the damping ratio ξ_q are designed so that the user can specify its values. In chapter *Symbols*, we introduce a dimensionless parameter f that includes both K_q and K. This is possible because only the ratio of K_q and K affects the system, but not the direct values itself. This enables us to let K_q be undefined. However, the simulation requires specific values to run for K_q. In chapter *Simulation* we show that using the dimensionless parameter f makes it possible to transfer the results to other stiffnesses of K_q. Unfortunately, we cannot find a variable that eliminates the user specified damping ratio ξ_q, so we have to agree on one value in order to run the analysis.

Parameters to be optimized are the stiffness K_η and the damping ratio ξ_η. Note that according to Figure 2.8 and 2.9, the damper is differently located dependent on using the VESπ or ESπ controller.

3.1 Range of Parameters

Since we are limited in the choice of parameters (we cannot test every parameter setting), we need to find parameters which are useful according to the hardware. Inspired by the testbench described in [Kep+18b, figure 5], we choose $M = 0.4639\text{kgm}^2$ for the link-side inertia. Motivated by the concept of TMD, which uses a very low mass ratio, we start the analysis with a inertia ratio $\mu = 1/20$. According to [Kep+18b], the testbench of an humanoid robot features an inertia ratio of $\mu = 3.30$ which is much higher. Thus, we increase the mass ratio for further analysis. Cropping the excitation frequency is due to the limitation of the control bandwidth of the link side. However, all natural frequencies of the system have to be included. We come to $0 \leq \omega \leq 6.6\text{Hz} = 41.5\text{rad}\,\text{s}^{-1}$. We choose a low damping ratio

of $\xi_q = 0.1$ to keep the ability to analyze the dynamic oscillation without directly being damped. We set $P_0 = 5\text{N m}$ which is a suitable value from experimental perspective. If this value is too low, friction influences the system too much. If this value too high, the motor torque reaches the limitation of 100N m according to [Kep+18b].

For the parameters to be optimized we also consider the mechanical model. The stiffness of spring K is in the range of $0 \leq K \leq 800\text{N m rad}^{-1}$ due to hardware limitation. Same for damping D_η (ESπ) and D (VESπ). Here, we can choose from the following range of the damping ratio of motor inertia B of $0 \leq \xi_\eta \leq 2$. The upper limitation comes from the claim, avoiding a supercritical damped element in the system because the robustness of the system decreases.

Still missing are the settings of the virtual spring K_q which we set to $K_q = 200\text{N m rad}^{-1}$ as this is a typical, average spring stiffness in the robotic system. We set the virtual damping ratio ξ_q of link inertia M to $\xi_q = 0.1$. With this setting of virtual spring and damper, we get an under critical damped system with an average choice of stiffness.

Considering that very small numbers close to 0 may cause numeric problems, we increase the minimum values from 0 to f.e. 0.1. Using the definitions of the symbols in Chapter and after rounding, we come to the following range of parameters:

$$\begin{aligned} M &= 0.4639\text{kgm}^2 \\ B &= 1.53\text{kgm}^2 \\ K_q &= 200\text{N m rad}^{-1} \\ \xi_q &= 0.1 \\ 0.1 \leq f &< 1.1 \\ 0.1 \leq \xi_\eta &< 2 \\ 0.01 \leq g &< 2 \end{aligned} \tag{3.2}$$

We reserve the possibility to change the range of parameters in every case, for example for focusing on an interesting area.

3.2 Analyzing the Amplitude Ratio

As a first objective, we want to analyze and reduce the amplitude ratio $\bar{q}$ of the link. A classical TMD is basically used to reduce the deflection of a mechanical system, like a tower or vibrating structures in cars. Chapter 2 describes the guideline, how to get optimal values for the tuning parameters. Following this idea, we want to find tuning parameters for the VESπ and ESπ system. To do this, we search for the *minimax amplitude* of the robot link. The *minimax amplitude* describes the minimum amplitude – due to

optimal tuning parameters – of the worst case (maximum amplitude) excitation frequency. This means, that independent of the frequency of the external torque, we can make sure that the amplitude of the robot link does not exceed a specific amplification.

The main difference between VESπ or ESπ controllers and TMD is basically the different setup: The two approaches have an additional spring and damper. But also, we have much higher inertia ratio. As the classical TMD features an inertia ratio $\mu \approx 1/20$, in our case we have to deal with an inertia ratio of $\mu \approx 3.30$. This is why we cannot just take the guideline of the TMD. Our first duty will be to check, if there even exist optimal parameters in a realistic range. Then we try to find a rule for the optimal parameters using an analytic approach. This enables us to implement a simple equation how to set the parameters. Finally, we extend the analysis with results of a simulation.

As we will discover later, in some cases there are no optimal parameters for the best minimax amplitude. In this case, we select specific excitation frequencies and define optimal parameters for specifically this excitation frequencies.

3.2.1 Derivation of the Oscillation Amplitude for VESπ closed-loop System

In this section, we want to develop an analytical approach for the amplitude of the link when excited with an harmonic torque. We use the closed-loop system of the VESπ controller applied on the VSEA drive system. Following the approach presented in [Har56, page 126], we install an harmonic torque at link side and expect a harmonic motion at link- and motor-side. We are interested in the amplitude of the harmonic motion.

We start with the equations of motion (2.16) and add an external excitation torque $P(t)$ (2.4) at inertia M. We use the complex approach (2.2) which yields

$$\begin{aligned} -\omega^2 \begin{bmatrix} B & 0 \\ 0 & M \end{bmatrix} \begin{bmatrix} \eta \\ q \end{bmatrix} e^{j\omega t} + j\omega \begin{bmatrix} D & -D \\ -D & D_q + D \end{bmatrix} \begin{bmatrix} \eta \\ q \end{bmatrix} e^{j\omega t} + \\ \begin{bmatrix} K & -K \\ -K & K_q + K \end{bmatrix} \begin{bmatrix} \eta \\ q \end{bmatrix} e^{j\omega t} = \begin{bmatrix} 0 \\ P(t) \end{bmatrix} e^{j\omega t} . \end{aligned} \tag{3.3}$$

As all derivatives are removed, we can shorten the equation as follows:

$$\begin{bmatrix} -\omega^2 B + j\omega D + K & -j\omega D - K \\ -j\omega D - K & -\omega^2 M + j\omega D_q + j\omega D + K_q + K \end{bmatrix} \begin{bmatrix} \underline{\eta}_0 \\ \underline{q}_0 \end{bmatrix} = \begin{bmatrix} 0 \\ P_0 \end{bmatrix} \tag{3.4}$$

Solving for q_0 and rearranging the differential equation leads to the complex harmonic excitation of coordinate q at link-side

$$\underline{q_0} = P_0 \frac{A_{eq}}{B_{eq}A_{eq} - C_{eq}^2} \tag{3.5}$$

$$\tag{3.6}$$

and coordinate η at motor-side

$$\underline{\eta_0} = P_0 \frac{C_{eq}}{C_{eq}^2 - B_{eq}A_{eq}} \tag{3.7}$$

$$\tag{3.8}$$

with

$$\begin{aligned} A_{eq} &:= -\omega^2 B + j\omega D + K \\ B_{eq} &:= -\omega^2 M + j\omega D_q + j\omega D + K_q + K \\ D_{eq} &:= -(j\omega D + K) \ . \end{aligned} \tag{3.9}$$

To transform the complex equations of motions into the amplitude, we consider the Pythagorean theorem as we did in Subsection 2.1.1. We bring both equations to the form

$$\underline{q_0} = P_0 \frac{E_{eq,q} + jF_{eq,q}}{G_{eq,q} + jH_{eq,q}} \tag{3.10}$$

and

$$\underline{\eta_0} = P_0 \frac{E_{eq,\eta} + jF_{eq,\eta}}{G_{eq,\eta} + jH_{eq,\eta}} \ . \tag{3.11}$$

Using them, we find the amplitude of the harmonic motion of coordinate q

$$q_0 = P_0 \sqrt{\frac{E_{eq,q}^2 + F_{eq,q}^2}{G_{eq,q}^2 + H_{eq,q}^2}} \tag{3.12}$$

with

$$\begin{aligned} E_{eq,q} &:= -\omega^2 B + K \\ F_{eq,q} &:= \omega D \\ G_{eq,q} &:= \omega^4 MB - \omega^2 BK_q - \omega^2 BK - \omega^2 D_q D - \omega^2 D^2 \\ &\quad - \omega^2 MK + K_q K + K^2 + \omega^2 D^2 - K^2 \\ H_{eq,q} &:= -\omega^3 D_q B - \omega^3 DB - \omega^3 MD + \omega DK_q + \omega D_q K \ . \end{aligned} \tag{3.13}$$

and coordinate η

$$\eta_0 = -P_0 \sqrt{\frac{E_{eq,\eta}^2 + F_{eq,\eta}^2}{G_{eq,\eta}^2 + H_{eq,\eta}^2}} \tag{3.14}$$

with

$$\begin{aligned}
E_{eq,\eta} &:= -K \\
F_{eq,\eta} &:= -\omega D \\
G_{eq,\eta} &:= -\omega^2 D^2 + K^2 - \omega^4 MB + \omega^2 BK_q + \omega^2 BK + \omega^2 D_q D \\
&\quad + \omega^2 D^2 + \omega^2 MK - K_q K - K^2 \\
H_{eq,\eta} &:= 2\omega DK + \omega^3 D_q B + \omega^3 DB + \omega^3 MD - \omega DK_q \\
&\quad - \omega DK - \omega D_q K - \omega DK \ .
\end{aligned} \tag{3.15}$$

In order to reduce the number of variables in the equation and to formulate the problem in dimensionless fashion, we introduce symbols which are presented in chapter *Symbols*. Applying them, we come to equations

$$\begin{aligned}
\bar{q} &= \sqrt{\frac{A_{eq,q}^2 + B_{eq,q}^2}{C_{eq,q}^2 + D_{eq,q}^2}} \\
A_{eq,q} &:= \mu f^2 - \mu g^2 \\
B_{eq,q} &:= 2g\xi_\eta \mu f \\
C_{eq,q} &:= -\mu^2 f^2 g^2 - 4\xi_\eta \mu f \xi_q g^2 - \mu f^2 g^2 + \\
&\quad \mu g^4 + \mu f^2 - \mu g^2 \\
D_{eq,q} &:= -2g^3 \mu^2 \xi_\eta f - 2g^3 \xi_\eta \mu f + 2\mu f^2 g \xi_q - \\
&\quad 2g^3 \mu \xi_q + 2g\xi_\eta \mu f
\end{aligned} \tag{3.16}$$

and

$$\begin{aligned}
\bar{\eta} &= \sqrt{\frac{A_{eq,\eta}^2 + B_{eq,\eta}^2}{C_{eq,\eta}^2 + D_{eq,\eta}^2}} \\
A_{eq,\eta} &:= 2\mu f g \xi_\eta \\
B_{eq,\eta} &:= \mu f^2 \\
C_{eq,\eta} &:= \mu^2 f^2 g^2 + 4\mu f g^2 \xi_\eta \xi_q + \mu f^2 g^2 - \\
&\quad \mu g^4 - \mu f^2 + \mu g^2 \\
D_{eq,\eta} &:= 2\mu^2 f g^3 \xi_\eta + 2\mu f g^3 \xi_\eta - 2\mu f^2 g \xi_q + \\
&\quad 2\mu g^3 \xi_q - 2\mu f g \xi_\eta \ .
\end{aligned} \tag{3.17}$$

What we get is a non-differential equation for the amplitude ratios $\bar{q}$ and $\bar{\eta}$ when exciting the system with a harmonic external torque at link side. The amplitude ratio $\bar{q}$ and $\bar{\eta}$ is the amplitude normalized with the static deflection q_{stat}. The symbol μ stands for the inertia ratio, by setting f we can change the natural frequency ratio and thereby the stiffness K. The

excitation frequency ratio g stands for the frequency of the external torque and ξ_η and ξ_q are the damping ratio of the two inertias.

Note that setting the damping ratio ξ_q to zero leads to (2.8) proposed by Den Hartog in [Har56]. This makes sense because this derivation of the VESπ controller is just extending the DenHartog's system (2.1) with an additional damper.

3.2.2 Derivation of the Oscillation Amplitude for ESπ closed-loop System

This chapter derives the equation for the amplitude of link coordinate q when the ESπ system is actuated with an external harmonic torque. The closed-loop system of SEA with ESπ controlling setup is represented by (2.20) which is extended with the harmonic excitation:

$$\begin{bmatrix} B & 0 \\ 0 & M \end{bmatrix} \begin{bmatrix} \ddot{\eta} \\ \ddot{q} \end{bmatrix} + \begin{bmatrix} D_\eta & 0 \\ 0 & D_q \end{bmatrix} \begin{bmatrix} \dot{\eta} \\ \dot{q} \end{bmatrix} + \begin{bmatrix} K & -K \\ -K & K + K_q \end{bmatrix} \begin{bmatrix} \eta \\ q \end{bmatrix} = \begin{bmatrix} 0 \\ P(t) \end{bmatrix} . \tag{3.18}$$

Using the complex approach (2.2) yields

$$\begin{aligned} -\omega^2 \begin{bmatrix} B & 0 \\ 0 & M \end{bmatrix} \begin{bmatrix} \eta_0 \\ q_0 \end{bmatrix} e^{j\omega t} + j\omega \begin{bmatrix} D_\eta & 0 \\ 0 & D_q \end{bmatrix} \begin{bmatrix} \eta_0 \\ q_0 \end{bmatrix} e^{j\omega t} + \\ \begin{bmatrix} K & -K \\ -K & K + K_q \end{bmatrix} \begin{bmatrix} \eta_0 \\ q_0 \end{bmatrix} e^{j\omega t} = \begin{bmatrix} 0 \\ P_0 \end{bmatrix} e^{j\omega t} . \end{aligned} \tag{3.19}$$

We can shorten the equation as follows:

$$\begin{bmatrix} -\omega^2 B + j\omega D_\eta + K & -K \\ -K & -\omega^2 M + j\omega D_q + K + K_q \end{bmatrix} \begin{bmatrix} \eta_0 \\ q_0 \end{bmatrix} = \begin{bmatrix} 0 \\ P_0 \end{bmatrix} . \tag{3.20}$$

Solving for q_0 and rearranging leads to the following complex equation:

$$\underline{q_0} = P_0 \frac{-B\,\omega^2 + j\,D_\eta\,\omega + K}{(-B\,\omega^2 + j\,D_\eta\,\omega + K)\,(-M\,\omega^2 + j\,D_q\,\omega + K + K_q) - K^2} . \tag{3.21}$$

We follow the same procedure for coordinate η:

$$\underline{\eta_0} = P_0 \frac{-K}{K^2 - (-\omega^2 M + j\omega D_q + K_q + K)(-\omega^2 B + j\omega D_\eta + K)} . \tag{3.22}$$

We bring both equations into the form of (3.10) and (3.11) to find the amplitudes of the harmonic motions of coordinate q:

$$\begin{aligned}
q_0 &= P_0 \sqrt{\frac{E_{eq,q}^2 + F_{eq,q}^2}{G_{eq,q}^2 + H_{eq,q}^2}} \\
E_{eq,q} &:= -B\,\omega^2 + K \\
F_{eq,q} &:= D_\eta\,\omega \\
G_{eq,q} &:= K\,K_q - D_\eta\,D_q\,\omega^2 - B\,K\,\omega^2 - B\,K_q\,\omega^2 + B\,M\,\omega^4 - K\,M\,\omega^2 \\
H_{eq,q} &:= D_\eta\,K\,\omega + D_\eta\,K_q\,\omega + D_q\,K\,\omega - B\,D_q\,\omega^3 - D_\eta\,M\,\omega^3
\end{aligned} \tag{3.23}$$

and coordinate η

$$\begin{aligned}
\eta_0 &= P_0 \sqrt{\frac{E_{eq,\eta}^2 + F_{eq,\eta}^2}{G_{eq,\eta}^2 + H_{eq,\eta}^2}} \\
E_{eq,\eta} &:= K \\
F_{eq,\eta} &:= 0 \\
G_{eq,\eta} &:= D_\eta\,D_q\,\omega^2 - K\,K_q + B\,K\,\omega^2 + B\,K_q\,\omega^2 - B\,M\,\omega^4 + K\,M\,\omega^2 \\
H_{eq,\eta} &:= B\,D_q\,\omega^3 - D_q\,K\,\omega - D_\eta\,K_q\,\omega - D_\eta\,K\,\omega + D_\eta\,M\,\omega^3\ .
\end{aligned} \tag{3.24}$$

Applying the definitions of the symbols presented in chapter *Symbols*, we come the following equations:

$$\begin{aligned}
\bar{q} &= \sqrt{\frac{A_{eq,q}^2 + B_{eq,q}^2}{C_{eq,q}^2 + D_{eq,q}^2}} \\
A_{eq,q} &:= \mu\,f^2 - \mu\,g^2 \\
B_{eq,q} &:= 2\,\xi_\eta \mu f g \\
C_{eq,q} &:= -\mu^2 f^2 g^2 - 4\,\xi_\eta\,\mu\,f \xi_q\,g^2 - \mu\,f^2 g^2 + \\
&\quad \mu\,g^4 + \mu\,f^2 - \mu\,g^2 \\
D_{eq,q} &:= 2\,\xi_\eta\,\mu^2 f^3 g - 2\,\xi_\eta\,\mu\,f g^3 + 2\,\xi_q\,\mu\,f^2 g - \\
&\quad 2\,\xi_q\,\mu\,g^3 + 2\,\xi_\eta\,\mu\,f g
\end{aligned} \tag{3.25}$$

and

$$
\begin{aligned}
\bar{\eta} &= \sqrt{\frac{A_{eq,\eta}^2}{C_{eq,\eta}^2 + D_{eq,\eta}^2}} \\
A_{eq,\eta} &:= \mu f^2 \\
C_{eq,\eta} &:= \mu^2 f^2 g^2 + 4\,\xi_\eta\,\mu\,f\xi_q\,g^2 + \mu\,f^2 g^2 - \\
&\quad \mu\,g^4 - \mu\,f^2 + \mu\,g^2 \\
D_{eq,\eta} &:= -2\,\xi_\eta\,\mu^2 f^3 g + 2\,\xi_\eta\,\mu\,f g^3 - 2\,\xi_q\,\mu\,f^2 g + \\
&\quad 2\,\xi_q\,\mu\,g^3 - 2\,\xi_\eta\,\mu\,f g\ .
\end{aligned}
\tag{3.26}
$$

3.3 Analysis of Maximum Motor Torque

Reducing the motor torque is a interesting factor for designing parameters. Less motor torque requires a smaller motor. This leads to decreasing robot mass and therefore to less power consumption. For analyzing the motor torque, we face the problem that the motor coordinate θ does not appear in the analytical closed-loop system of neither VESπ nor ESπ controller. This is why we use the simulation to obtain information about the motor behavior. The simulation directly provides the amplitude of the motor torque τ_m.

As we excite the system with an harmonic torque, we assume a sine-wave correlating behavior of the motor torque $\tau_m(t)$. For us, the amplitude is the interesting factor, as we are interested in the maximum value. This is why we consider the maximum $\tau_{m,0}$ of the motor torque. Similar to the argumentation we did for the amplitude ratio $\bar{q}$, we normalize the motor torque amplitude $\tau_{m,0}$ with the excitation torque amplitude P_0. This leads to the dimensionless *motor torque amplitude ratio*

$$
\bar{\tau}_m = \frac{\tau_{m,0}}{P_0}\ . \tag{3.27}
$$

For the analysis over a selected range of excitation frequencies, we introduce the maximum motor torque ratio $\bar{\tau}_{m,max}$. This is the maximum motor torque amplitude ratio in a selected range of exciting frequencies.

3.4 Power Analysis

The power analysis is essential for mobile robots that are dependent on small energy storage. Using a strongly simplified model of the motor and the mechanical model, ohmic loss and core loss are not considered. Thus, this analysis only focuses on the mechanical energy injected into the system by the motor.

In order to achieve time-invariant data, we consider the *mean power over one period* of the excitation torque instead of the current power. As

shown in (3.1), the external torque is a harmonic sine-function with the frequency ω. This leads to periodic signals of the system when transient response is neglected. Thus, the power signals are also periodic signals of period $t_{end}-t_{start}$. The measurement of the *average mechanical motor power* $P_{\mathrm{M,mean}}$ is performed using [WF16, eq. 16 and 17] as

$$P_{\mathrm{M,mean}} = \frac{1}{t_{end} - t_{start}} \int_{t_{start}}^{t_{\mathrm{end}}} f(t)dt \tag{3.28}$$

where

$$f(t) = \begin{cases} \bar{\tau}_m \dot{\theta} & \bar{\tau}_m \dot{\theta} > 0 \\ 0 & \text{else} \end{cases} .$$

The variables t_{start} and t_{end} are the time of the start and end of the period. For considering the *maximum average mechanical motor power* over a range of excitation frequencies, $P_{\mathrm{M,mean,max}}$ is introduced. This value provides the average power consumption for the worst excitation frequency case.

The breaking power $P_{\mathrm{br,mean}}$ appears when the motor acts as a generator. In this case, power is extracted from the mechanical system and transformed into electrical power. Inspired by [WF16, eq. 18 and 19], the *mean mechanical breaking power* over one period is calculated by

$$P_{\mathrm{br,mean}} = \frac{1}{t_{end} - t_{start}} \int_{t_{start}}^{t_{\mathrm{end}}} g(t)dt \tag{3.29}$$

where

$$g(t) = \begin{cases} 0 & \text{else} \\ \bar{\tau}_m \dot{\theta} & \bar{\tau}_m \dot{\theta} < 0 \end{cases} .$$

If the system is able to recuperate energy, all breaking power will flow back into the energy storage and can be used again. Otherwise, the motor or motor control will transform all breaking energy into heat which means that it cannot be returned into the energy storage. This analysis assumes that the system cannot restore the breaking power.

In contrast to the torque of the excitation, the injected power differs depending on the choice of f and ξ_η. We can see this fact from the definition of the injected power

$$P_{\mathrm{ext,mean}} = \frac{1}{t_{end} - t_{start}} \int_{t_{start}}^{t_{end}} \tau_{ext}(t)\, \dot{q}(t)\, dt \ . \tag{3.30}$$

This shows, that the injected power is dependent on the rotational velocity $\dot{q}$, which is dependent on f and ξ_η.

In order to implement a useful comparison and to create a result independent from the injected power, we introduce the normalized power

$$P_{norm,1} = \frac{P_{M,mean}}{P_{ext,mean}} \ . \tag{3.31}$$

Chapter 4

Analysis of VSEA under VESπ control

This chapter adopts the methods described in Chapter 3 and analyzes the VSEA-system actuated with the VESπ control approach. As we have seen in Section 2.3, we can describe the closed-loop behavior as a mechanical mass-spring-damper-system due to the mechanical inspired control approach. We separate the analysis in two parts: The analysis over a chosen range of excitation frequencies provides the worst case amplitude. The analysis for a specific excitation frequency includes more information as we consider selected frequency separately.

4.1 Analysis for a Range of Excitation Frequencies

Here, our focus is on a suitable range of excitation frequencies, which means that we always consider the worst case scenario. This is done by a frequency analysis where all excitation frequencies in an useful selected range are applied on the system. We take the maximum value of amplitude ratio, motor torque or others. To tag this value, we add a *max* to the variable's subscript. This method is useful when the excitation frequency is not known or when impacts are applied on the mechanical system.

4.1.1 Analysis of Link Amplitude Ratio

We focus on the frequency response of VESπ system shown in Figure 4.1 with several damping ratios ξ_η. We want to point out that this system has a mass ratio of $\mu = 1/20$. In contrast to that, a typical robot link and motor features a much higher mass ratio μ. While comparing this figure with the frequency response of the TMD in Figure 2.2, we find a similar picture. Due to the additional damping ratio ξ_q, all amplitudes are more flattened. When $\xi_\eta = 0$, we see two resonant frequencies. As there is no damping in

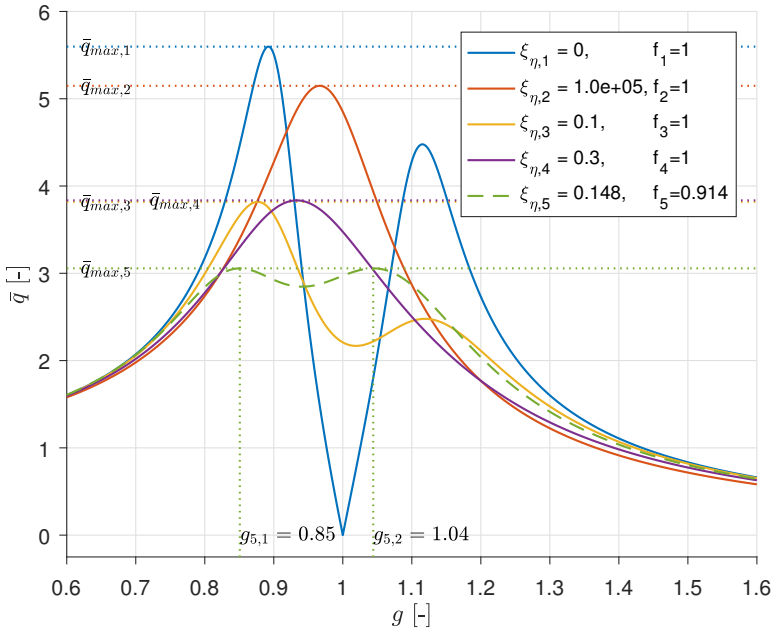

Figure 4.1: This graph shows the link-side *amplitude ratio* $\bar{q}$ of the ESπ system when excited with the *excitation frequency ratio* g. With different *damping ratios* ξ_η, the frequency response changes fundamentally. The natural frequency ratio f is set to 0, except of curve 5. For us, the *maximum amplitude ratio* $\bar{q}_{max}$, labeled as $\bar{q}_{max,1\ldots5}$, is the most important result. The excitation frequency of the maximum amplitude of curve 5 is illustrated as $g_{5,1\ldots2}$. For this analysis, we considered the mass ratio $\mu = 1/20$.

between the inertias, they act like a two-mass system featuring two resonant frequencies. When $\xi_\eta = 10^5$, the two-mass system behaves like an one-mass system. Due to the highly damped connection between masses B and M, they tend to stick together. As a result of the effective mass $M + B$, the main mode is slightly lower than we would expect it to be with only mass M. The cases $\xi_\eta = 0.1$ and $\xi_\eta = 0.3$ illustrate two damping ratios. The graph with $\xi_\eta = 0.1$ is characterized by two nicely damped natural modes with a maximum amplitude ratio $\bar{q}_{max,3}$. When setting $\xi_\eta = 0.3$, the frequency response features only one maximum amplitude ratio $\bar{q}_{max,4}$. Somewhere in the middle, there is an optimal value for the damping ratio ξ_η so that the maximum value of the amplitude ratio is smallest. Curve 5 illustrates the frequency response with perfectly tuned parameters. As we will see later, there is no other choice of parameters that features a lower *maximum amplitude ratio*.

It is noticeable that in contrast to the frequency response of the classical TMD in Figure 2.2, there are no intersection points where all curves meet. As the intersection points are the precondition to derive optimal parameters for TMD, we cannot use the method of the TMD to find a rule, how to set the optimal tuning parameters. This is why we have to run a numerical

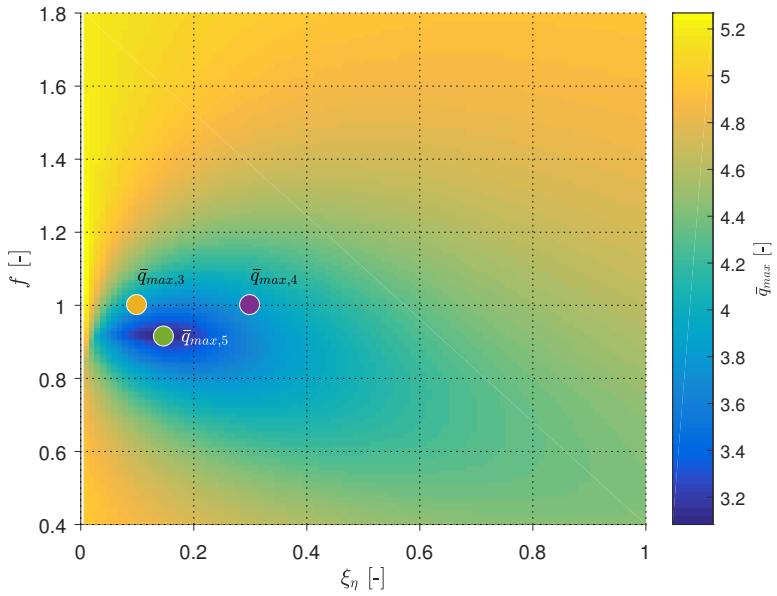

Figure 4.2: This graph shows the link-side *maximum amplitude ratio* $\bar{q}_{max}$ of the ESπ system. We took the values of $\bar{q}_{max,1...5}$ (Figure 4.1) and drew them in this graph at the corresponding position of the *natural frequency ratio* f and the *damping ratio* ξ_η. As $\bar{q}_{max,1}$ and $\bar{q}_{max,2}$ feature parameters outside of the graph, they don't appear here. The color depicts the value of the *maximum amplitude ratio* $\bar{q}_{max}$. Overall, this graph shows the effect of f and ξ_η on $\bar{q}_{max}$. We used the mass ratio $\mu = 1/20$.

analysis to find optimal parameters for the minimum $\bar{q}_{max}$ using (3.16).

We take the maximum amplitude ratios of Figure 4.1 $\bar{q}_{max,1...5}$ and draw them into a graph at the corresponding position, according to f and ξ_η. As $\bar{q}_{max,1}$ and $\bar{q}_{max,2}$ feature parameters outside of the graph, they do not appear in the graph. We get Figure 4.2. It shows the maximum amplitude ratio $\bar{q}_{max}$ when mass ratio $\mu = 1/20$ for a wide range of the tuning parameters f and ξ_η. It is easy to recognize that there is a clear global minimum for a specific choice of f and ξ_η, exactly where we found $\bar{q}_{max,5}$. We have created this plot using (3.16) for the VESπ system. Referring to chapter *Symbols*, f includes the stiffness K of the spring between masses M and B and ξ_η is the damping ratio of inertia B.

As we already introduced the value for the *minimax* amplitude ratio, we increase the inertia ratio μ. Figure 4.3 shows the optimal values for the tuning parameters f and ξ_η for each inertia ratio. The horizontal axis depicts the inertia ratio μ. There are several graphs in the chart. First, we focus on the excitation frequency ratio g, where the system reaches its maximum amplitude. The dimensionless value g depicts the excitation frequency ratio. There are two lines which points at the fact that for the considered range of mass ratio μ, there are two excitation frequencies for the optimal tuned system where it reaches the maximum amplitude. We can clearly see this

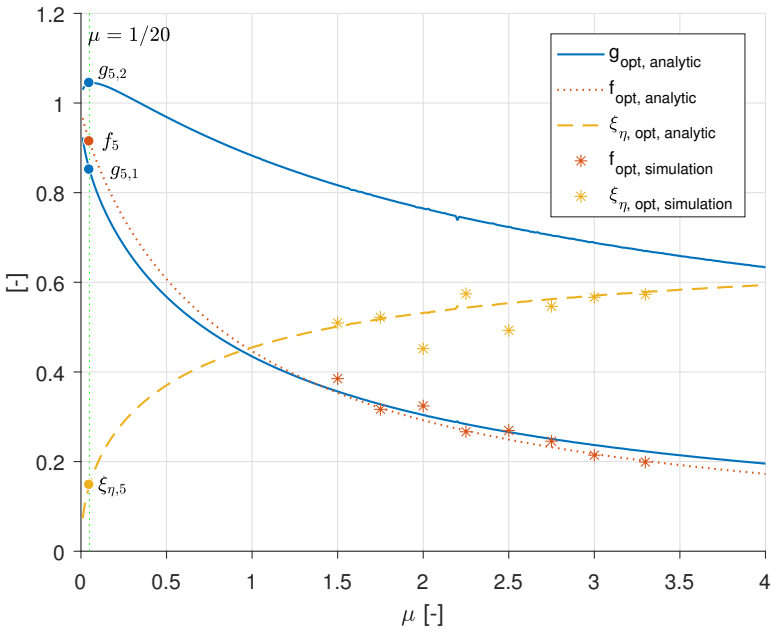

Figure 4.3: This graph presents the optimal parameters f and ξ_η of the VESπ system for a range of the mass ratio μ. It depicts the two excitation frequency ratio g where the maximum amplitude occurs. As shown in graph 4.4, a perfectly tuned system always features two maximum excitation frequencies. Here, the graph indicates the optimal values for the natural frequency f (which correlates with the stiffness K) and the damping ratio ξ_η for the mass ratio μ and damping ratio $\xi_q = 0.1$. We added the values $g_{5,1\ldots2}$, f_5 and $\xi_{\eta,5}$ of $\mu = 1/20$ as shown in graph 4.4. The stars represent results from the simulation.

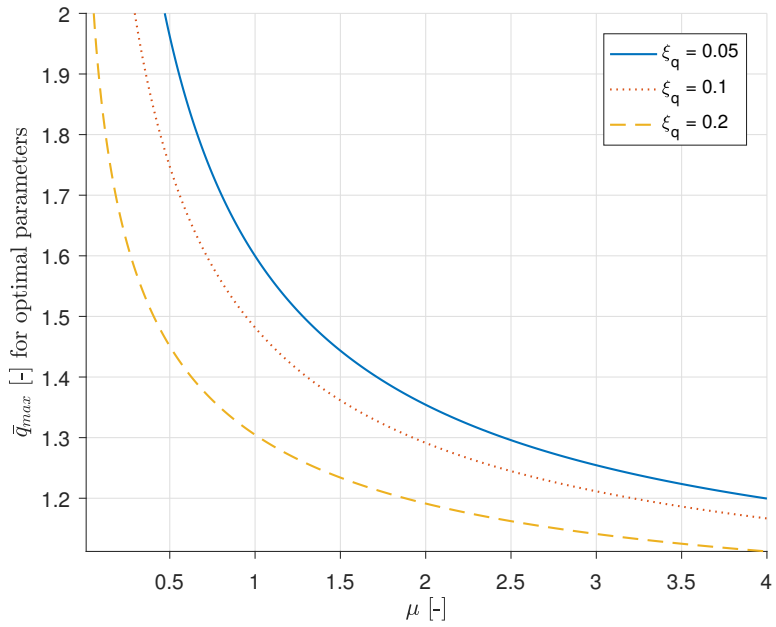

Figure 4.4: The normalized amplitude ratio $\bar{q}$ of the VESπ system with optimal parameters and with several damping ratios ξ_q. A range of the mass ratio μ is considered.

fact in Figure 4.1.

Second, we focus on the optimal value for f which is a dimensionless parameter for the spring stiffness K. Third, we focus on the best parameter for the damping ratio ξ_η. The graph was created using the analytical equation presented in Subsection 3.2.1. As additional information, the stars represent the same result, but using the simulation tool (introduced in Chapter B). The stars belong to the line with the same color.

Figures 4.4 shows the minimax amplitude ratio $\bar{q}_{max}$ when using the optimal tuning parameters of the VESπ system. There are several graphs in the chart. Each of them stands for a damping ratio ξ_q and were created using the analytical equation presented in Subsection 3.2.1. The figure shows that the minimax amplitude decreases when increasing the mass ratio μ.

For practical purposes it might be easier to follow a simple design equation for choosing the parameters. This is why the Matlab *curve fitting Tool Box* was used to create a equation based on the analytical system. An optimum value can only be found when ξ_q satisfies

$$\boxed{\xi_{q,\mathrm{VES}\pi} < 0.6\ .} \tag{4.1}$$

The optimum value for the natural frequency ratio f was created with *Matlab curve fitting toolbox*. The validation is made using the R-square, which is the square of the correlation between the real value and the calculated value

of the equation. This equation features a R-square of 0.9991.

$$\boxed{\begin{aligned} f_{opt,\mathrm{VES}\pi} &= \frac{1 + a\,\xi_q}{1 + b\,\mu + c\,\xi_q} \\ a &:= -1.437 \\ b &:= 1.033 \\ c &:= -1.031 \end{aligned}} \tag{4.2}$$

which correlates with the joint stiffness K:

$$K_{opt} = f_{opt}^2\,\frac{K_q B}{M}\ . \tag{4.3}$$

The optimum value for the damping ratio ξ_η was created using *Matlab curve fitting tool* with a R-square of 0.9971.

$$\boxed{\begin{aligned} \xi_{\eta,opt,\mathrm{VES}\pi} &= \sqrt{\frac{3\,\mu}{a\,(1+\mu)} + b\,\xi_q^2} \\ a &:= 7.029 \\ b &:= 0.07705 \end{aligned}} \tag{4.4}$$

which also can be translated into the damping value D_η using the definitions of the symbols in chapter *Symbols* and the following relation:

$$D_{\eta,opt} = 2\xi_{\eta,opt}\sqrt{BK} \tag{4.5}$$

For having a closer look on mass ratio $\mu = 3.30$, we created Figure 4.5. This heatmap illustrates the maximum amplitude ratio $\bar{q}_{max}$ for changing values of f (stiffness K of spring) and ξ_η (damping ratio). It is easy to see that there is a minimum at $f \approx 0.2$ and $\xi_\eta \approx 0.58$. This can also be seen at the optimal tuning parameters in graph 4.3 at $\mu = 3.30$.

4.1.2 Analysis of Maximum Motor Torque

In many cases, the maximum amplitude of $\tau_m(t)$ is important. Here, we analyze the system considering the normalized motor torque amplitude ratio $\bar{\tau}_{m,max}$. Figure 4.6 represents $\bar{\tau}_{m,max}$ over a selected range of excitation frequencies for the mass ratio $\mu = 3.30$. It was created using the simulation illustrated in Chapter B. This graph provides an overview of the motor's behavior for a range of tuning parameters. It shows that there is a minimum at $f \approx 0.4$ and $\xi_\eta \approx 0.6$.

As we can see from Figure 4.6, the motor torque increases sharply for small values of f. This is due to a very soft stiffness K when f is low. As the torque at link side is created due to the rotational difference $K(\theta - q)$, the motor has to accelerate very fast to create a sudden torque. When the spring stiffness K is low, the motor has to accelerate even faster which results in a high motor torque.

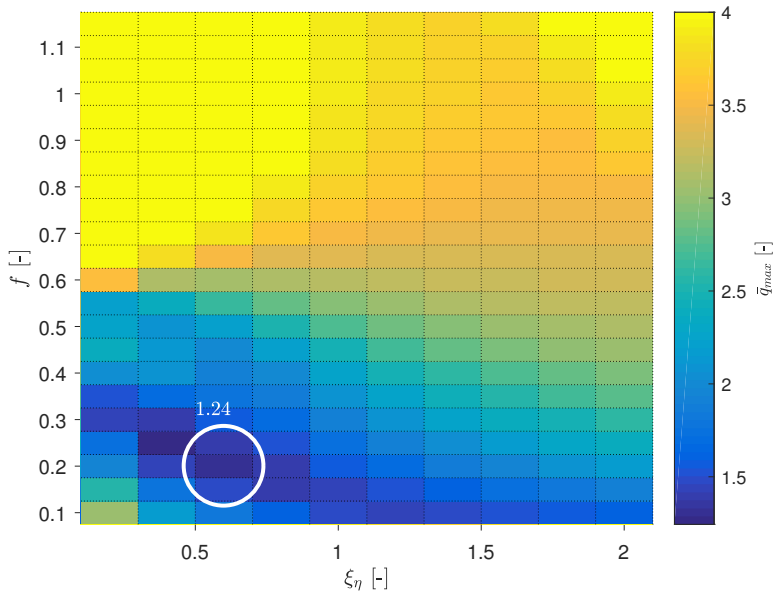

Figure 4.5: This graph illustrates the maximum value of the amplitude ratio $\bar{q}_{max}$ in a selected range of excitation frequencies. For this simulation results, $\xi_q = 0.1$ for the damping ratio and the standard setting presented in Chapter B was used. The inertia ratio μ was set to 3.30.

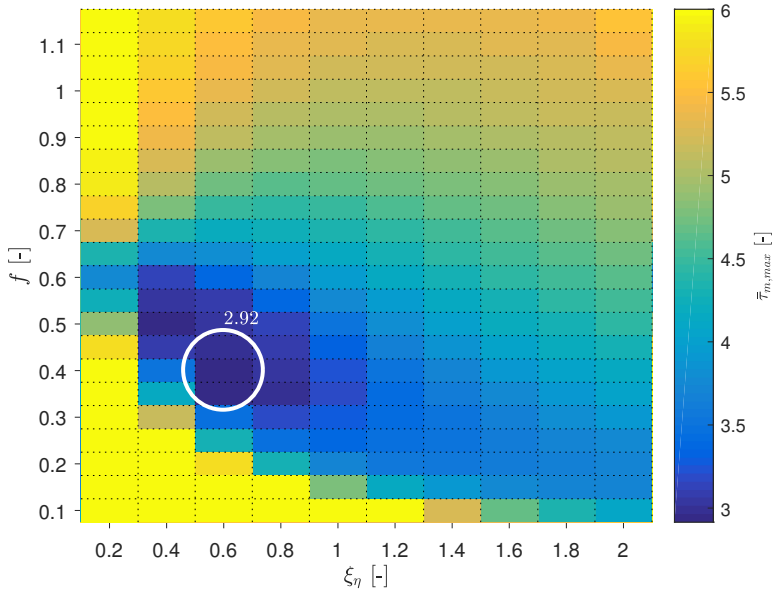

Figure 4.6: The maximum normalized motor torque amplitude ratio $\bar{\tau}_{m,max}$ for the VESπ control with a mass ratio of $\mu = 3.30$ is shown for a the natural frequency ratio f and damping ratio ξ_η. We choose the maximum value over a selected range of excitation frequencies. For this simulation results we used $\xi_q = 0.1$ for the damping ratio and the standard setting presented in Chapter B.

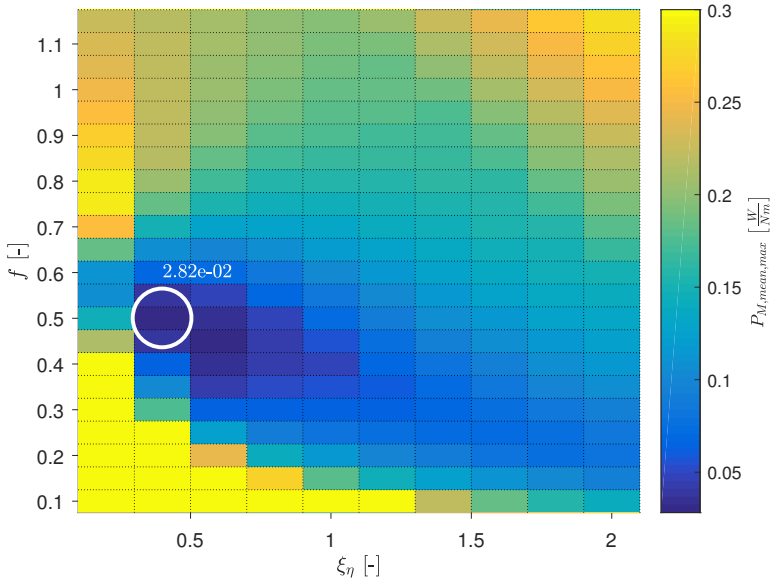

Figure 4.7: The maximum value for the consumed power $P_{\mathrm{M,mean,max}}$ for the VESπ control with a mass ratio of $\mu = 3.30$ is shown. The axis are the natural frequency ratio f and the damping ratio ξ_η. We choose the maximum value over a selected range of excitation frequencies. For this simulation results we used $\xi_q = 0.1$ for the damping ratio and the standard setting presented in Chapter B.

4.1.3 Power Analysis

Following the concept of the reduction of the motor's consumed energy shown in Subsection 3.4, we present the results of the simulation. Figure 4.7 gives an advice how to choose parameters f and ξ_η in order to reduce the motor's power $P_{\mathrm{M,mean,max}}$. In order to create the plot, we used a simulation as explained in Chapter B with a mass ratio $\mu = 3.30$ and a damping ratio $\xi_q = 0.1$. As we already did in the previous graphs, we select the maximum value over all considered excitation frequencies.

Due to the fact that for every choice of tuning parameters the system injects a different amount of energy, the motor power $P_{M,mean}$ is normalized with the external power $P_{ext,mean}$. Following (3.31), we run a simulation. Figure 4.8 illustrates the results of this attempt. This plot is a heatmap of the maximum normalized power consumption over a selected range of excitation frequencies with changing parameters f and ξ_η. This graph features a clear minimum of the normalized consuming power $P_{norm,1,max}$ for the tuning parameters ξ_η and f. In the left lower corner, the normalized motor power rises sharply. Considering the results for specific excitation frequencies in Section 4.2 shows that this values are dominated from lower excitation frequencies.

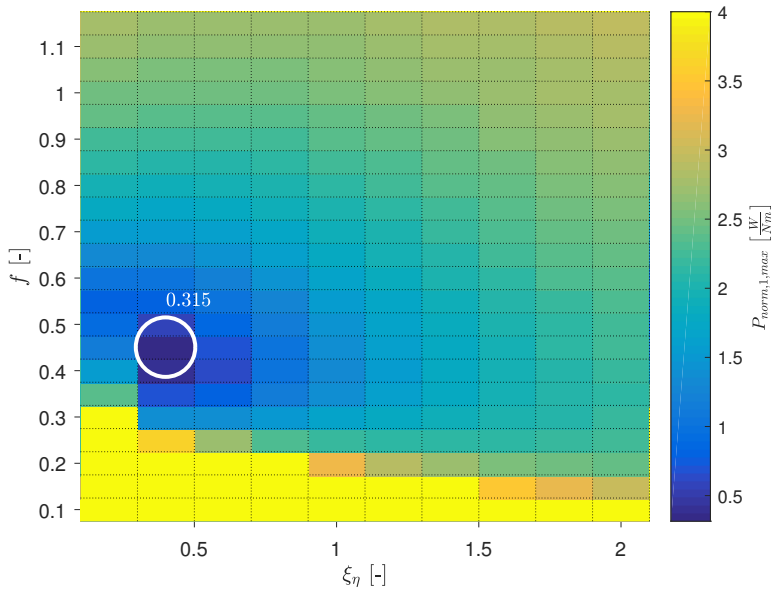

Figure 4.8: The maximum value for the normalized power $P_{norm,1}$ for the VESπ control with a mass ratio of $\mu = 3.30$ is shown. We choose the maximum value over a selected range of excitation frequencies and draw them for a the natural frequency ratio f and damping ratio ξ_η. For this simulation results we used $\xi_q = 0.1$ for the damping ratio and the standard setting presented in Chapter B.

4.2 Analysis for Specific Excitation Frequencies

Here, our focus is on specific excitation frequencies, which means we define the interesting excitation frequency first and than, later on, we find optimal parameters for several objectives. This method is useful when the system is being influenced with a specific excitation frequency.

To get an idea how the amplitude ratio $\bar{q}_{max}$ behaves for specific excitation frequencies, we focus on Figure A.1 in the appendix. The minimum value of $\bar{q}_{max}$ is located on different tuning parameters dependent on the selected excitation frequency. A trend for lower natural frequency ratios f as optimal setting for lower excitation frequencies g can be seen. All damping ratios ξ_η are optimal for very low values. This is a crucial finding as the open loop system always features damping in form of friction. This result highlights the fact that a reduction of the friction leads to better performance in terms of less vibration. It additionally reveals that the amplitude ratio $\bar{q}_{max}$ can be very little, even lower than 1.

Figure A.2 in the appendix shows the normalized torque $\bar{\tau}_m$ applied to the system by the motor. As we can see from the low resolution, this values are created using the simulation with a relatively high time consumption. There is a minimum for the motor torque in each excitation frequency that can be selected by choosing the corresponding tuning values f and ξ_η.

Figure A.3 in the appendix shows the mean power consumption $P_{M,mean}$ of the motor. This gives an advice how to choose tuning parameters f and ξ_η when the power consumption is to be minimized.

A similar value we observe in Figure A.4. There, we normalize the motor's power consumption by the injected power due to the external deflection. Then we come to the values of $P_{norm,1}$.

Chapter 5

Analysis of SEA under ESπ control

This chapter adopts the methods described in Chapter 3 and analyze the SEA-system actuated with the ESπ control approach. Following the procedure in Chapter 4, we divide the analysis in two parts: The analysis over a chosen range of excitation frequencies provides the worst case amplitude. The analysis for a specific excitation frequency includes more information as we consider every frequency separately. We focus on a frequency and parameter range as explained in Chapter 4.

5.1 Analysis for a Range of Excitation Frequencies

Here, our focus is on a range of excitation frequencies and we always consider the worst case scenario. This is done by a frequency analysis where all excitation frequencies in the selected range are applied on the system. We take the maximum value of amplitude ratio, motor torque or others.

5.1.1 Analysis of Link Amplitude Ratio

As we did in Chapter 5, we start with the frequency response of ESπ system shown in Figure 5.1 with several damping ratios ξ_η. The frequency analysis is very similar to Figure 4.1. This is why we refer to its explanation.

We take the maximum amplitude ratios of Figure 5.1 $\bar{q}_{max,1\ldots5}$ and draw them into a graph at the corresponding position according to their f and ξ_η. As $\bar{q}_{max,1}$ and $\bar{q}_{max,2}$ feature parameters outside of the graph, they don't appear here. What we get is illustrated in Figure 5.2. It shows the maximum amplitude ratio $\bar{q}_{max}$ when mass ratio $\mu = 1/20$ for a wide range of the tuning parameters f and ξ_η. We have created this plot using (3.25) for the ESπ system. The ESπ controller differs from the VESπ controller

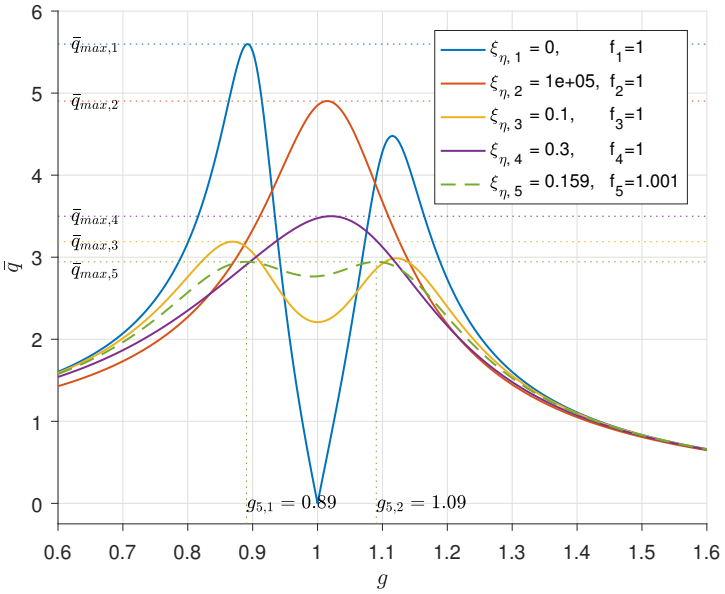

Figure 5.1: The graph shows the *amplitude ratio* $\bar{q}$ of the ESπ system when excited with the *excitation frequency ratio* g. With different *damping ratios* ξ_η, the frequency response changes fundamentally. The natural frequency ratio f is set to 1, except of curve 5. The *maximum amplitude ratio* $\bar{q}_{max}$ over the selected range of g is the most important result. This is why we labeled the *maximum amplitude ratio* for each setting of ξ_η as $\bar{q}_{max,1\ldots5}$. We used the mass ratio $\mu = 1/20$.

due to a different position of the damper. The different setting will lead to a fundamental different behavior.

Increasing parameter f (which is equal to increasing stiffness K) and increasing damping ratio ξ_η lead to a decreasing amplitude ratio $\bar{q}_{max}$ of the link which can be seen in the dark blue area. This means, the higher f and ξ_η, the lower the amplitude ratio of the link is. This behavior is dominated by the damping ratio ξ_η of inertia B. As this damper is connected to the environment, with raising damping ratio ξ_η, more torque is necessary to move inertia B. This effect influences inertia M more, when f is high, as this spring connects inertia M and B. This means when both parameter ξ_η and f are high, inertia M with coordinate q can hardly be moved. We prove this assumption using (3.23) with

$$\lim_{K,D_\eta \to \infty,\infty} P_0 \sqrt{\frac{A_{eq,q}^2 + B_{eq,q}^2}{C_{eq,q}^2 + D_{eq,q}^2}} = 0 \ . \tag{5.1}$$

This shows that the amplitude q_0 is zero in this case, whatever the other parameters are.

This property makes it hard to find a suitable minimum with useful parameters. Analyzing TMD and VESπ systems, we could observe an obvious minimum in the amplitude ratio which is the location of the optimal tuning

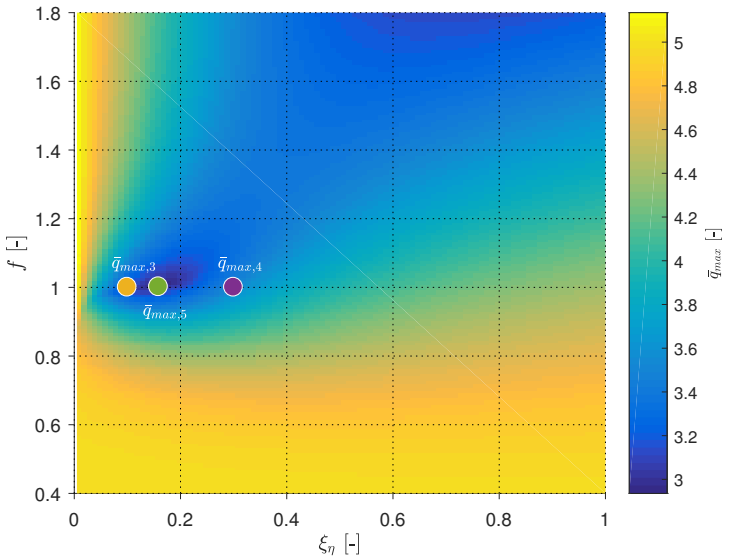

Figure 5.2: This graph shows the *maximum amplitude ratio* $\bar{q}_{max}$ of the ESπ system. We took the values of $\bar{q}_{max,1\ldots5}$ (Figure 5.1) and drew them in this graph at the corresponding position of the *natural frequency ratio* f and the *damping ratio* ξ_η. As $\bar{q}_{max,1}$ and $\bar{q}_{max,2}$ feature parameters outside of the graph, they don't appear here. The color depicts the value of the *maximum amplitude ratio*. Overall, this graph shows the effect of f and ξ_η on $\bar{q}_{max}$. We used the mass ratio $\mu = 1/20$ and increased the parameter range for better illustration.

parameters. Here – using the ESπ controller – we can only find a local minimum that is marked with a green circle in graph 5.2. The global minimum is located in outside of the graph.

Why don't we just use a very big f and ξ_η to fulfill our aim reducing the amplitude as best as possible?

The idea of a impedance control is the ability to choose the dynamic interaction between a manipulator and its environment. This interaction is controlled by the virtual spring K_q and the virtual damper D_q causing ξ_q. As long as the other two parameters K and ξ_η are small, they don't interfere much in the impedance behavior. We want to avoid stiffness K and damper ξ_η dominating the systems behavior. This is why we want them to keep as small as possible and this is why we don't want to follow the global minimum in Figure 5.2 which is located at very big f and ξ_η. So we are chasing for the local minimum, which is marked with a circle in the graph.

As we have already introduced the value for the *minimax* amplitude ratio, we increase the inertia ratio μ. Figure 5.3 shows the optimal values for the tuning parameters f and ξ_η for each inertia ratio. The horizontal axis depicts the inertia ratio μ. There are several graphs in the chart. First, we can read the excitation frequency ratio g where the system reaches its maximum amplitude. There are two lines which points at the fact that for

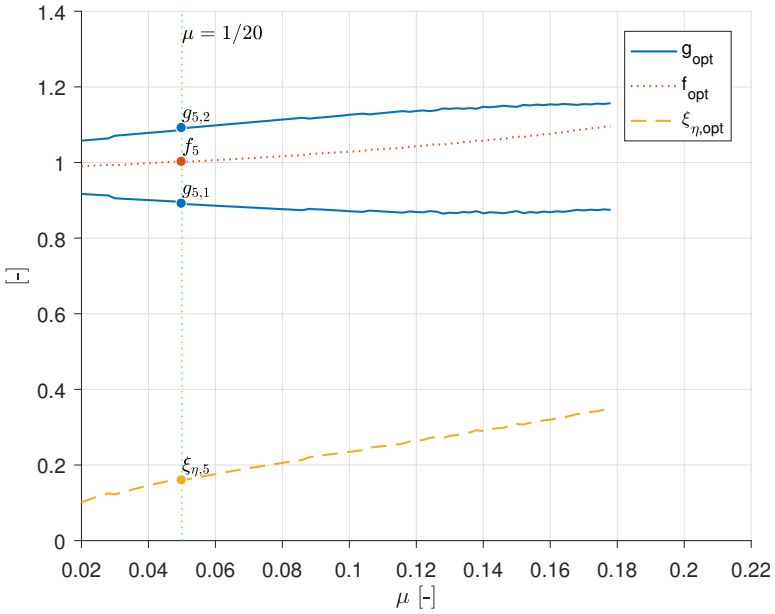

Figure 5.3: This graph presents the optimal parameters f and ξ_η of the ESπ system for a range of the mass ratio μ. It shows, at what excitation frequency ratio g the maximum amplitude occurs. As illustrated in graph 5.4, a perfectly tuned system always features two maximum excitation frequencies for every set of tuned parameters. Here, the graph indicates the optimal values for the natural frequency f (which correlates with the stiffness K) and the damping ratio ξ_η for the mass ratio μ and damping ratio $\xi_q = 0.1$. We added the values $g_{5,1\ldots2}$, f_5 and $\xi_{\eta,5}$ of $\mu = 1/20$ as shown in graph 5.4.

the considered mass ratio μ there are two frequencies where the optimal tuned system reaches the maximum amplitude.

Second, we read the best fitting value for f. Third, we read the best parameter for the damping ratio ξ_η. The graph was created using the analytical equation presented in Subsection 3.2.2.

The most important issue we see is that the local minimum vanishes when μ is big. There are no optimal parameters anymore when the mass ratio $\mu > 0.18$ for small ξ_q. Figure 5.3 illustrates this fact as the curves stop at $\mu \approx 0.18$. This can graphically interpreted using Figure 5.2. For rising μ, the local minimum elevates until it is higher than the transition to the global minimum. From this mass ratio μ on, the local minimum has vanished and this is why there are no optimum parameters anymore.

Figures 5.4 shows the minimax amplitude ratio $\bar{q}_{max}$ when using the optimal tuning parameters of the ESπ system. There are several graphs in the chart. Each of them stands for a damping ratio ξ_q and were created using the analytical equation presented in Subsection 3.2.2. The figure shows that the minimax amplitude decreases when increasing the mass ratio μ.

We can find an equation that describes the maximum possible ξ_q and μ:

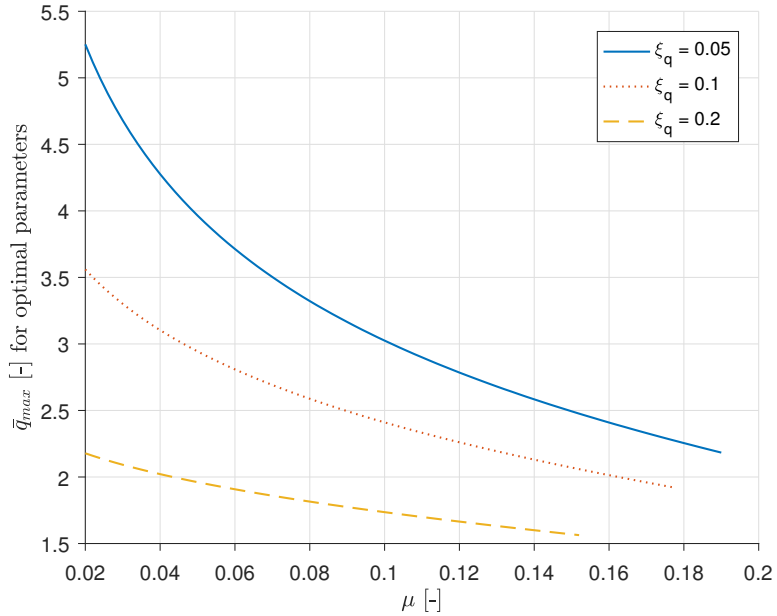

Figure 5.4: The normalized amplitude ratio $\bar{q}$ of the ESπ system with optimal parameters and with several damping ratios ξ_q. The values are indicated within a range of mass ratio μ. From a specific value of the mass ratio μ on, no optimal set of parameter can be found. In the graph, this is indicated with an ending line.

$$\begin{aligned} &0 < \mu \leq 0.2 \\ &\xi_{q,\mathrm{ES}pi} < -\frac{50}{12}\mu + 0.83 \ . \end{aligned} \tag{5.2}$$

Having limitations (5.2) in mind, we find an equation that describes the optimum values for f and ξ_q. They were created using the analytical approach presented in Subsection 3.2.2 and Matlab *curve fitting Tool Box*. First, we propose the optimum value for the natural frequency ratio f. This approach features R-square of 0.9958.

$$\begin{aligned} f_{opt,ES\pi} &= \frac{1 + a\,\mu + b\,\xi_q}{1 + c\,\mu + d\,\xi_q} \\ a &:= -1.465 \\ b &:= -1.45 \\ c &:= -1.924 \\ d &:= -1.164 \ , \end{aligned} \tag{5.3}$$

which can be transformed into the stiffness K of the spring between the two inertias B and M using the definitions of the symbols in chapter *Symbols*:

$$K_{opt} = f_{opt}^2 \frac{BK_q}{M} \ . \tag{5.4}$$

The optimum value for the damping ratio ξ_η was found with *Matlab curve fitting Tool Box* featuring a R-square of 0.9951.

$$\begin{aligned} \xi_{\eta,opt,ES\pi} &= (a\,\xi_q + b\,\mu + c)\mu^d \\ a &:= 0.986 \\ b &:= 1.054 \\ c &:= 0.484 \\ d &:= 0.4634 \ , \end{aligned} \tag{5.5}$$

which also can be transformed into the damping value D_η using the definitions of the symbols in chapter *Symbols* and the following relation:

$$D_{\eta,opt} = 2\xi_{\eta,opt}\sqrt{KB} \ . \tag{5.6}$$

In Figure 5.5 we want to demonstrate the maximum amplitude ratio $\bar{q}_{max}$ for a mass ratio $\mu = 3.30$. It is easy to see that there is a minimum but only at high values for f and ξ_η. This is why it is impossible to find optimal tuning parameters for hight inertia ratios.

5.1.2 Analysis of Maximum Control Effort

We come to the same conclusion when looking at the maximum control effort. Figure 5.6 represents the maximum normalized motor torque amplitude ratio $\bar{\tau}_{m,max}$ over a selected range of excitation frequencies for the mass ratio $\mu = 3.30$. It was created using the simulation illustrated in Chapter B in the appendix. As we expect from our experience with the link amplitude ratio $\bar{q}$, the analysis of the motor torque shows that there is no minimum with suitable parameters.

5.1.3 Power Analysis

Following the aim reducing the motor's consumed energy shown in Subsection 3.4, we present the results of the simulation. Figure 5.7 shows the consumed mean power by the motor $P_{\mathrm{M,mean}}$ and proves that there is again no minimum. To create the plot, we used a simulation as explained in Chapter B with a mass ratio $\mu = 3.30$ and a damping ratio $\xi_q = 0.1$.

Figure 5.8 is a heatmap of the maximum normalized power $P_{norm,1,max}$ over the selected range of excitation frequencies with changing parameters f and ξ_η, using the simulation. This graph depicts the conclusion, that there is no minimum within the selected range of tuning parameters.

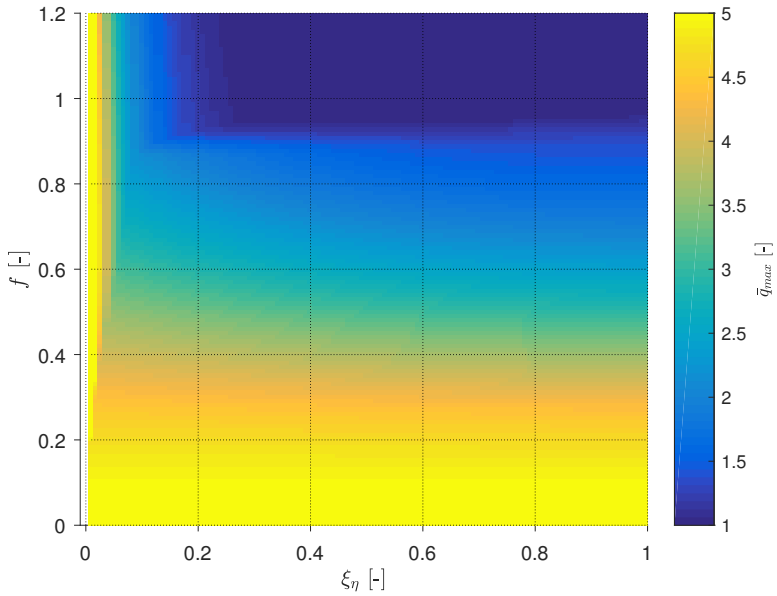

Figure 5.5: The maximum amplitude ratio $\bar{q}_{max}$ for the ESπ controller with a mass ratio of $\mu = 3.30$ is shown over the selected frequency ratio range. The values are drawn according to the natural frequency ratio f and damping ratio ξ_η. For this analytical results we used $\xi_q = 0.1$ for the damping ratio. It is obvious that increasing parameters f and ξ_η always leads to decreasing amplitude of q.

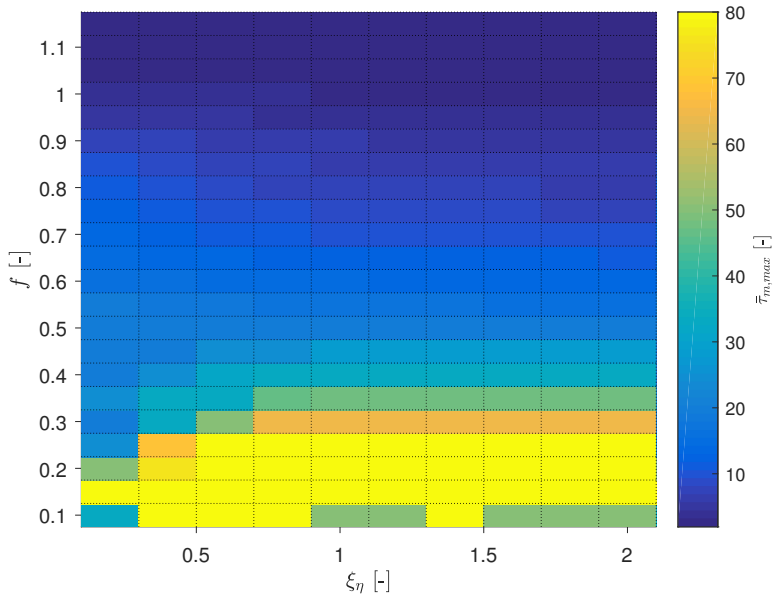

Figure 5.6: The maximum value for the motor torque $\tau_{m,max}$ for the ESπ controller with a mass ratio of $\mu = 3.30$ is shown. We choose the maximum value over a selected range of excitation frequencies. The values are drawn according to the natural frequency ratio f and damping ratio ξ_η. For this simulation results we used $\xi_q = 0.1$ for the damping ratio and the standard setting presented in Chapter B.

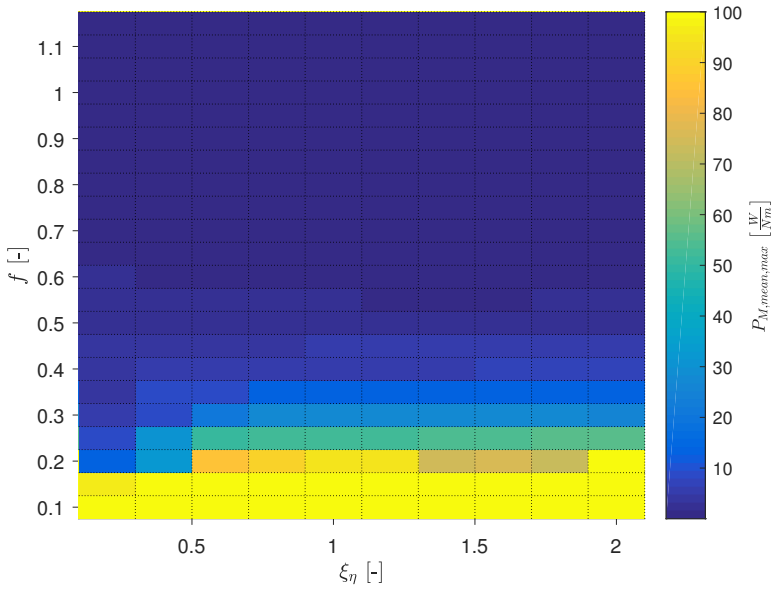

Figure 5.7: The maximum value for the consumed power $P_{\mathrm{M,mean}}$ for the ESπ controller with a mass ratio of $\mu = 3.30$ is shown. We choose the maximum value over a selected range of excitation frequencies. The values are drawn according to the natural frequency ratio f and damping ratio ξ_η. For this simulation results, we used $\xi_q = 0.1$ for the damping ratio and the standard setting presented in Chapter B.

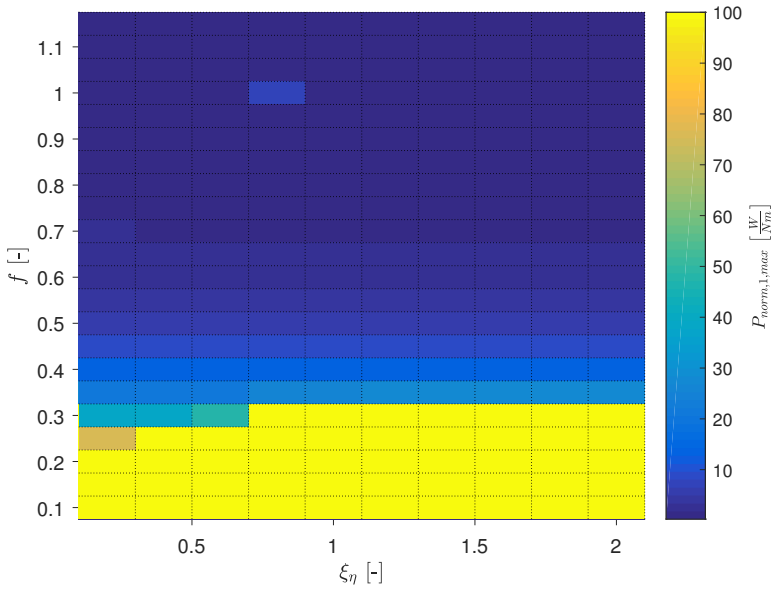

Figure 5.8: The maximum value for the normalized power $P_{norm,1}$ for the ESπ controller with a mass ratio of $\mu = 3.30$ is shown. We choose the maximum value over a selected range of excitation frequencies. The values are drawn according to the natural frequency ratio f and damping ratio ξ_η. For this simulation results, we used $\xi_q = 0.1$ for the damping ratio and the standard setting presented in Chapter B.

5.2 Analysis for Specific Excitation Frequencies

As we have seen in Section 5.1, it is fundamental to consider specific excitation frequencies when using the ESπ system. Considering the maximum value over the selected range of frequencies, it is impossible to find optimal parameters. Now, we want to focus on specific excitation frequencies so that we can extract useful hints, how to choose the parameters f and ξ_η.

To get an idea how the amplitude ratio $\bar{q}_{max}$ behaves for specific excitation frequencies using the ESπ controller, we focus on Figure A.5 in the appendix. The optimal values are dependent on the selected excitation frequency. Most interesting is what happens when increasing frequency of the external torque. Then, the minimum moves to bigger values of f and a new maximum appears parallel to the vertical axis. It additionally reveals that the amplitude ratio $\bar{q}_{max}$ can be very little, even lower than 1.

Figure A.6 in the appendix shows the normalized torque $\bar{\tau}_m$ applied to the system by the motor, using the ESπ controller. As we can see from the low resolution, this values are created using the simulation with a relatively high time consumption. There is a minimum for the motor torque in each excitation frequency that can be selected by choosing the corresponding tuning values f and ξ_η.

Figure A.7 in the appendix shows the mean power consumption $P_{M,mean}$ of the motor. This gives an advice how to choose tuning parameters f and ξ_η when the power consumption is to be minimized.

A similar value we observe in Figure A.8. As explained in Chapter 3, we normalize the motor's power consumption by the injected power. Then we come to the values of $P_{norm,1}$.

Chapter 6

Conclusion and Outlook

6.1 Conclusion

In this work we developed methods to analyze the compliant robot drives actuated with the controllers VESπ and ESπ. We stated several cost functions concerning performance and power efficiency: The link's vibration, the torque of the motor and the power consumption. We concentrated on the case with external, harmonic torque excitation at link side and without tracking. This means, we excited the robot link with a sine-shaped torque and demanded the controller to hold the position.

Taking advantage of the mechanical motivated design of the control approaches allows us to replace the closed-loop system with a mechanical oscillator. Inspired by the theory of the classical TMD, we defined several tuning parameters that shape the behavior of the system. The other parameters are either meant to choose by the user or values dependent on the hardware design. For this work, these parameters are set to standard values.

We derived an analytical model of each of the two substitution systems – VESπ and ESπ – representing the closed-loop behavior. This method provides an equation that describes the amplitude ratio of the harmonic link movement. For validation purpose and for extracting additional information – like motor torque and power consumption – we ran a simulation in *Matlab Simulink*. We used a simplified dynamic model of the mechanical open-loop system actuated with the VESπ and ESπ controller.

As a main result in this work, the effects of the tuning parameters on the VESπ system behavior were investigated. Additionally, a guideline for the parameters' optimal choice was developed, considering changing design parameters in regard to minimize the cost functions.

The analysis of the ESπ controller leads to the conclusion that the optimal tuning parameters do not exist. They are set to unrealistic and ineffectual values when decreasing the cost functions. This is why we focused on specific excitation frequencies for the analysis. We defined the frequency of

the external torque first and then set up the tuning parameters. With this strategy, we provided an guideline for the parameters' effects on the cost functions.

All things considered, our findings indicate that the results are highly dependent on the inertia ratio of the motor reflected inertia and the robot link inertia. As with stretched out robot arm the link inertia is much higher than in bent position, the tuning parameters have to be continuously adjusted. As shown, the power consumption can vary in a wide range so that a wrong settings of the tuning parameters can lead to much higher energy consumption, which is highly relevant for mobile robotics.

6.2 Outlook

In this work, we presented a guideline for setting up the tuning parameters for minimizing the maximal amplitude ratio. We considered several mass ratios. Future research should further develop similar guidelines for other cost functions, especially for varying mass ratios. They should include motor power consumption with consideration of recuperation and ohmic loss. This approach would provides information about a wider range of robot configuration.

With the restriction on a harmonic external torque at link side, we created a rather unrealistic scenario for normal robot movements. Usually, robots movements include tracking and complex trajectories. We faced the challenge to reduce the general movement of a robot system to a simplified and easy to analyze movement case. However, there is a wide field of possible movements that can be analyzed for optimizing the tuning parameters. This could be simple joint rotation or more complex tracking tasks of the control system. As a following challenge, other simplified movements can be outlined and analyzed. As a long term aim, a guideline can be developed that automatically choose the best fitting tuning parameters for every situation. This would decrease the power consumption and improve the performance.

Other simplifications made in this work due to reduction of complexity lead to uncertainties in the result. Many compliant robots (e.g. David from DLR) feature nonlinear properties. As a future work, nonlinear spring characteristic can be assumed and analyzed, as well as nonlinear motor characteristic and a more precise friction model. Additionally, limitation of spring's and damper's torsion should be considered to widen the field of possible robot system that are represented in the analysis.

Apart from that, an easy to evaluate description of the expected power consumption can be developed. A simulation – similar to the one that already exist – can help to estimate the energy needed for a moving task. As mobile robots are dependent on a light and small energy source, an estimation and minimization of the energy consumption is important.

Appendix A

Appendix

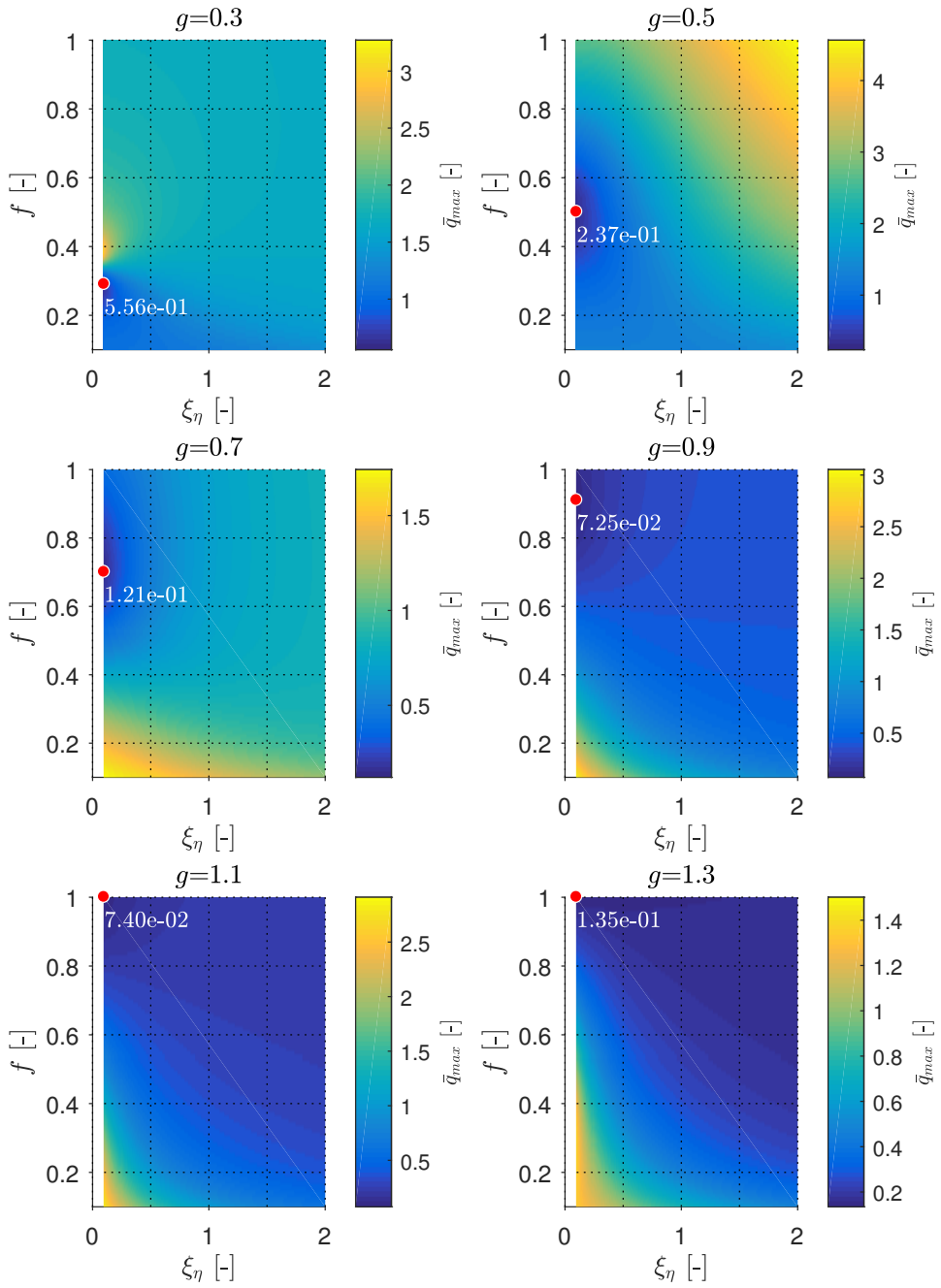

Figure A.1: The amplitude $\bar{q}_{max}$ for VESπ with a mass ratio of $\mu = 3.30$ is shown. The results can be selected for specific excitation frequency ratios g. The values are drawn according to the natural frequency ratio f and damping ratio ξ_η. For this simulation results, we used $\xi_q = 0.1$ for the damping ratio and the standard setting presented in Chapter B.

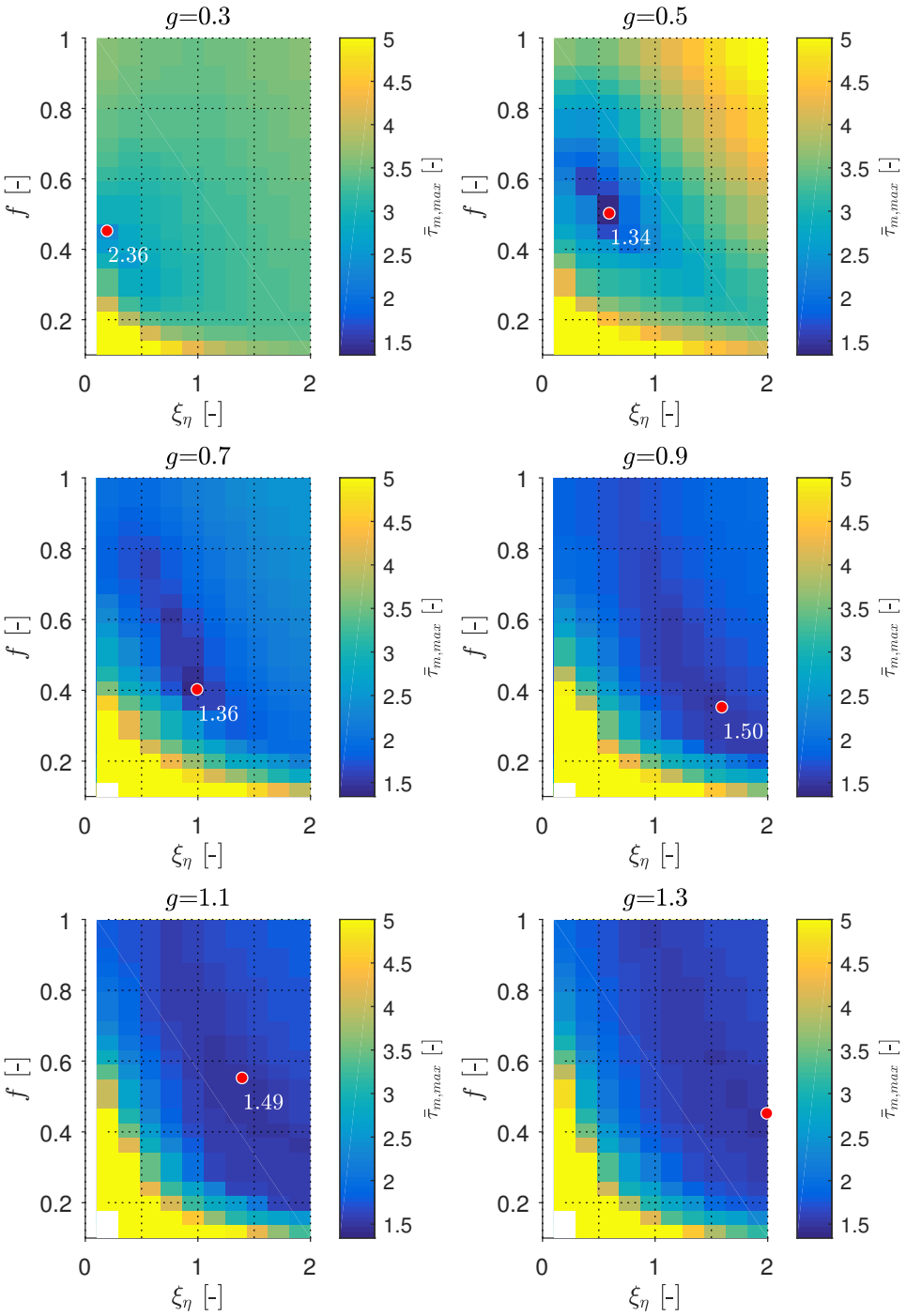

Figure A.2: The control effort $\tau_{m,max}$ for VESπ with a mass ratio of $\mu = 3.30$ is shown. The results can be selected for specific excitation frequency ratios g. The values are drawn according to the natural frequency ratio f and damping ratio ξ_η. For this simulation results, we used $\xi_q = 0.1$ for the damping ratio and the standard setting presented in Chapter B.

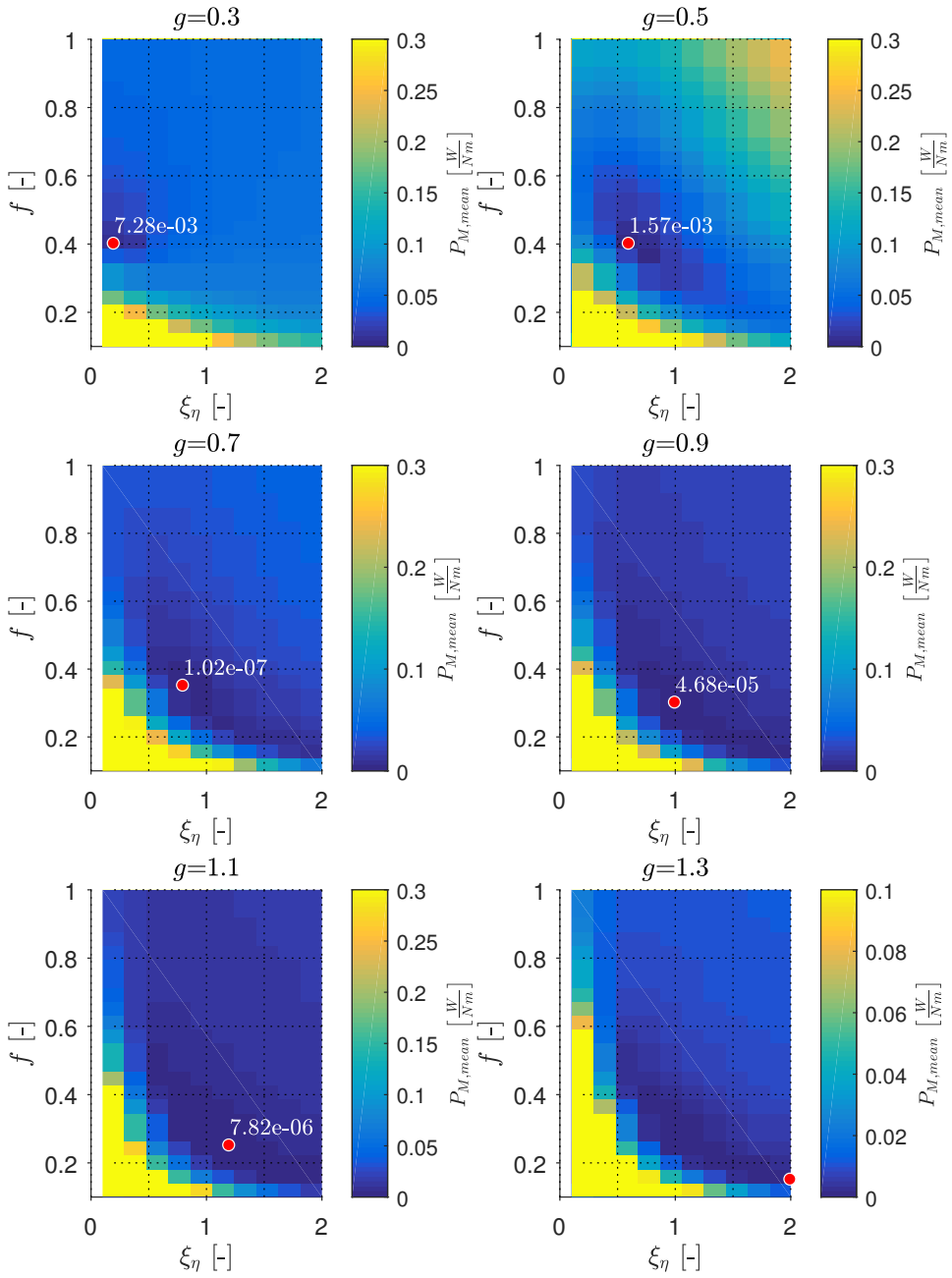

Figure A.3: The motor's power $P_{\mathrm{M,mean}}$ for VESπ with a mass ratio of $\mu = 3.30$ is shown. The results can be selected for specific excitation frequency ratios g. The values are drawn according to the natural frequency ratio f and damping ratio ξ_η. For this simulation results, we used $\xi_q = 0.1$ for the damping ratio and the standard setting presented in Chapter B.

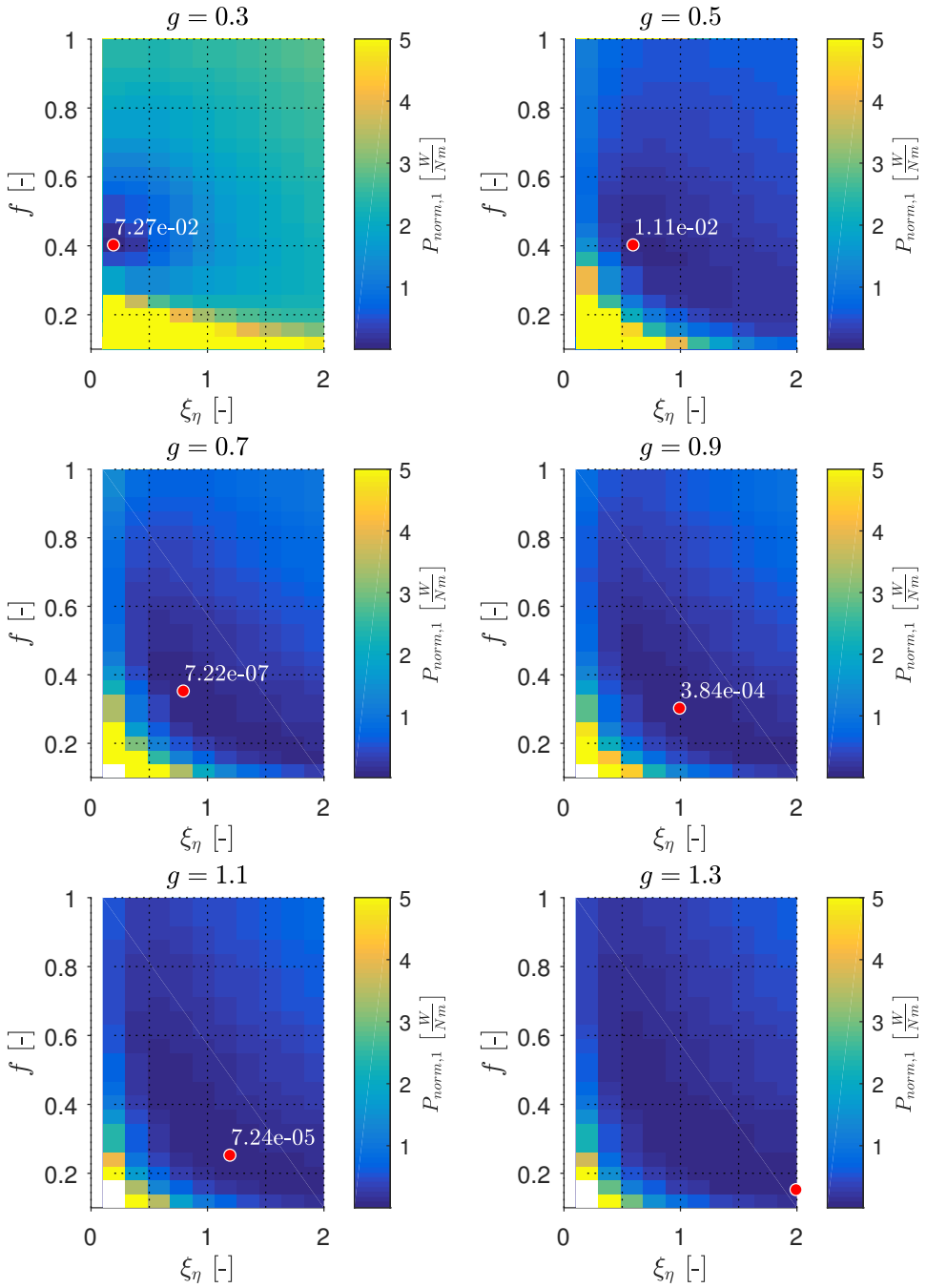

Figure A.4: The normalized motor's power $P_{norm,1}$ for VESπ with a mass ratio of $\mu = 3.30$ is shown. The results can be selected for specific excitation frequency ratios g. The values are drawn according to the natural frequency ratio f and damping ratio ξ_η. For this simulation results, we used $\xi_q = 0.1$ for the damping ratio and the standard setting presented in Chapter B.

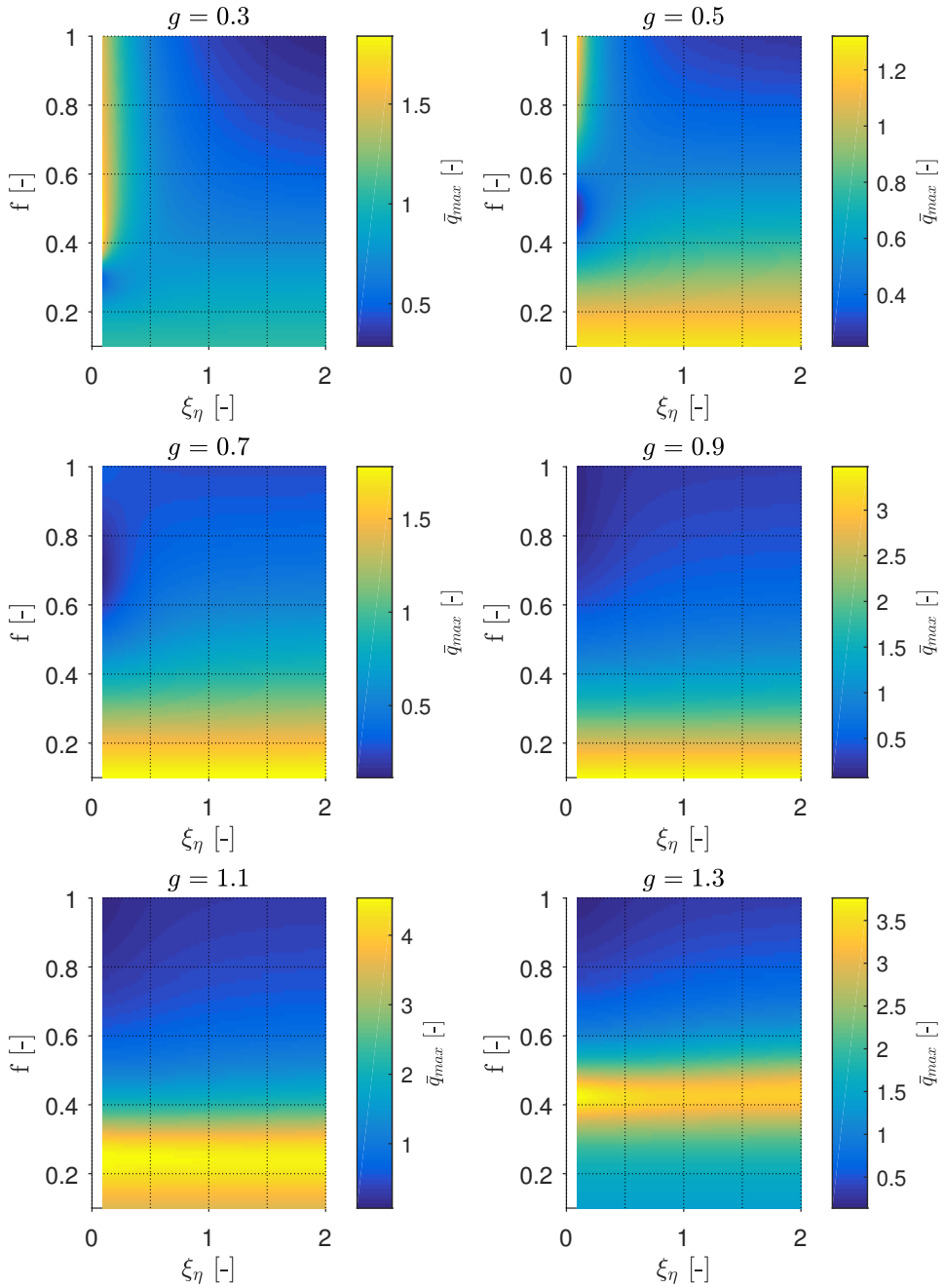

Figure A.5: The amplitude $\bar{q}_{max}$ for ESπ with a mass ratio of $\mu = 3.30$ is shown. The results can be selected for specific excitation frequency ratios g. The values are drawn according to the natural frequency ratio f and damping ratio ξ_η. For this simulation results, we used $\xi_q = 0.1$ for the damping ratio and the standard setting presented in Chapter B.

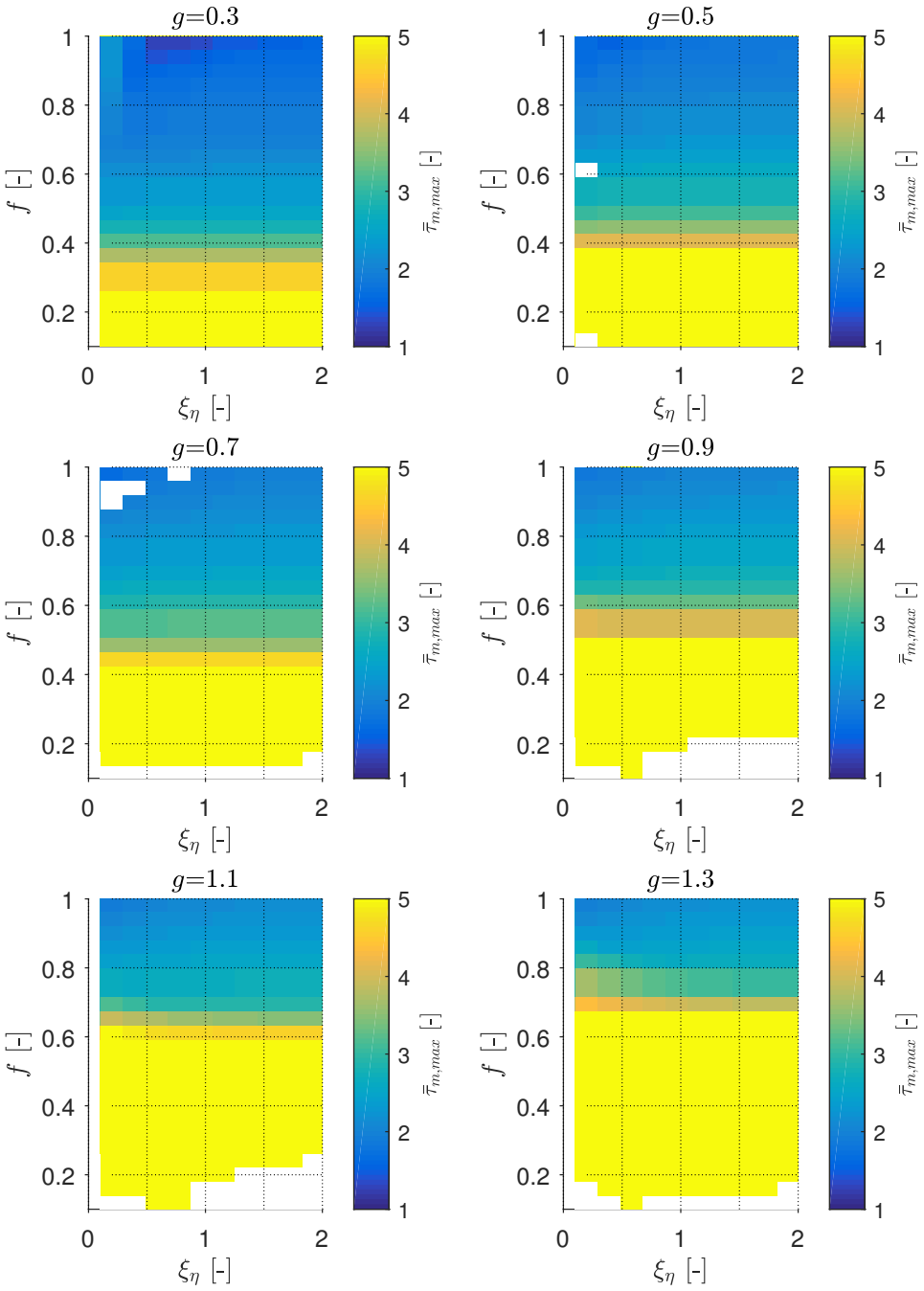

Figure A.6: The control effort $\tau_{m,max}$ for ESπ with a mass ratio of $\mu = 3.30$ is shown. The results can be selected for specific excitation frequency ratios g. The values are drawn according to the natural frequency ratio f and damping ratio ξ_η. For this simulation results, we used $\xi_q = 0.1$ for the damping ratio and the standard setting presented in Chapter B.

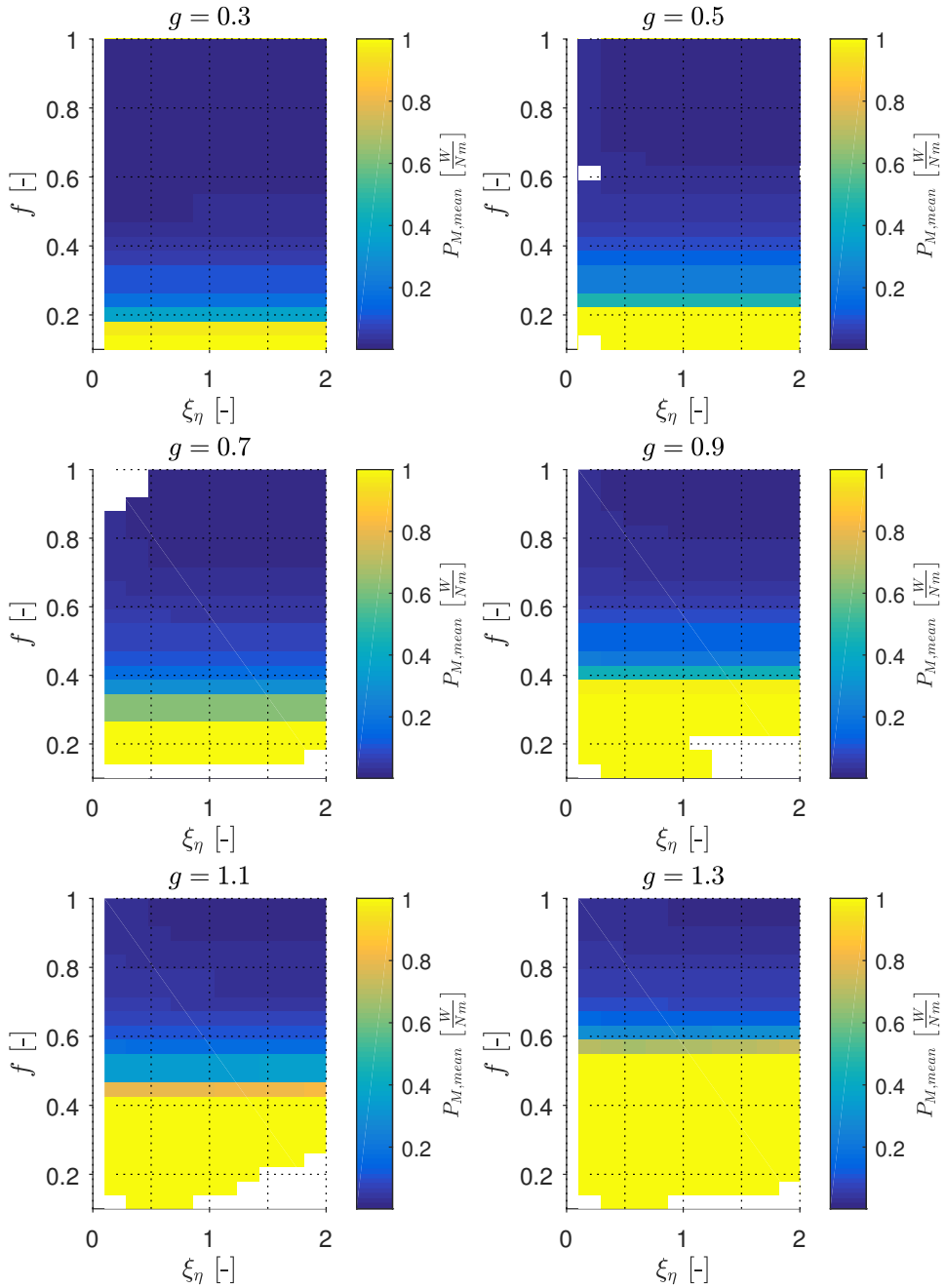

Figure A.7: The motor's power $P_{\mathrm{M,mean}}$ for ESπ with a mass ratio of $\mu = 3.30$ is shown. The results can be selected for specific excitation frequency ratios g. The values are drawn according to the natural frequency ratio f and damping ratio ξ_η. For this simulation results, we used $\xi_q = 0.1$ for the damping ratio and the standard setting presented in Chapter B.

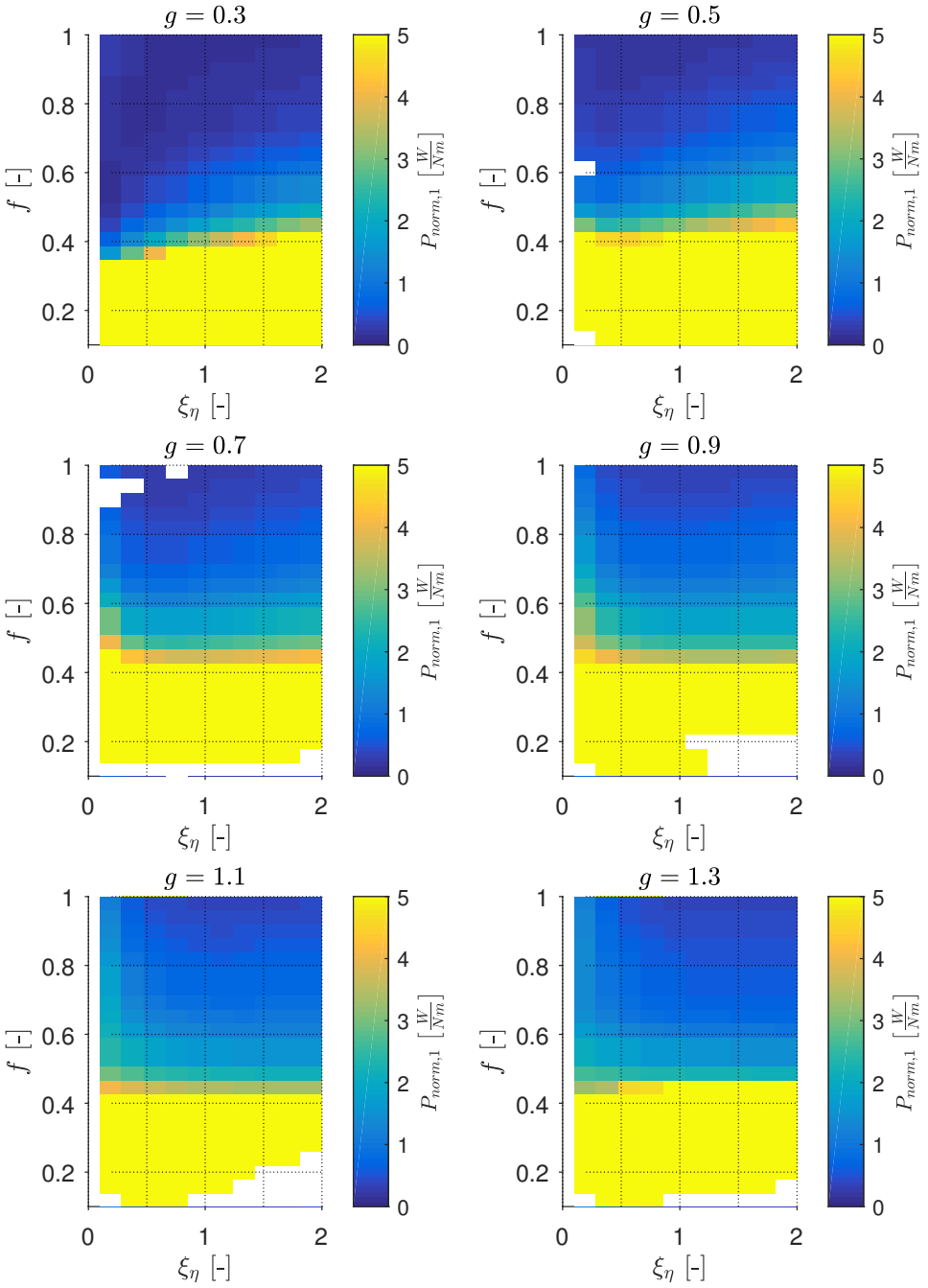

Figure A.8: The normalized motor's power $P_{norm,1}$ for ESπ with a mass ratio of $\mu = 3.30$ is shown. The results can be selected for specific excitation frequency ratios g. The values are drawn according to the natural frequency ratio f and damping ratio ξ_η. For this simulation results we used $\xi_q = 0.1$ for the damping ratio and the standard setting presented in Chapter B.

Appendix B

Simulation

The simulation is a useful tool to easily test hundreds of different sets of parameters. We have developed a script that allows to test a range of parameters by running a lot of serial simulations. Basically, the model represents the mechanical drive system (VSEA or SEA) and actuates it with the controller (VESπ or ESπ). We expect the simulation to act similar to the closed-loop system of the controllers, presented in Section 2.3.

This chapter briefly reviews the simulation system we use for the analysis and presents the buildup of the simulation. As this simulation includes friction of the gear, we identify parameters that match the original behavior of the gear system.

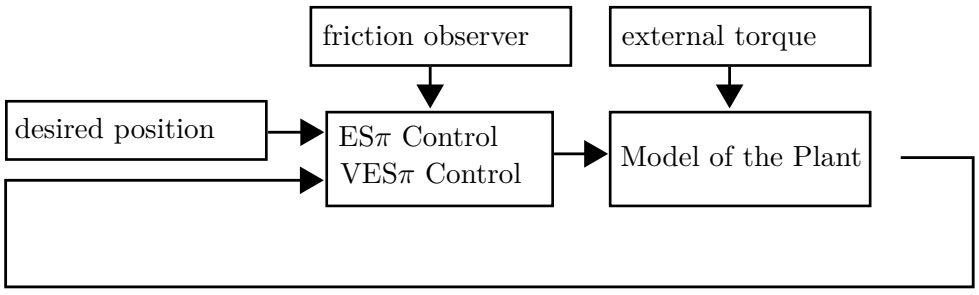

Figure B.1: The structure of the simulation consists of the plant which is actuated by the controlling part. The external torque influences the plant.

In Figure B.1, the structure of the simulation is shown. The *Model of the Plant* – which is the VSEA and SEA – is actuated by the VESπ or ESπ control. The *external torque* excitation points at the *Model of the Plant*. It is actuated by the VESπ or ESπ controller which processes the *desired position* of the link. In our case, we set the *desired position* to zero. The

analytical approach evaluates the closed-loop behavior directly while the simulation computes the open-loop system separately to the VESπ or ESπ controller (or any other controller).

We use the simulation to compare the analytical approach presented in Subsection 3.2 with the results of the simulation. Due to friction, numerical errors and time-dependent errors, the results can differ. We additionally extract internal information which cannot be calculated via the analytical approach. For example, the control effort τ_m is not part of the closed-loop system and thus can only be evaluated with the open-loop system which is used in the simulation.

B.1 Structure

The simulation structure consists of three main components: The motor with gear drive, the link with changeable inertia and a coupling mechanism in between. The motor is simplified as an inertia and a torque input. We ignore internal ohmic loss and any nonlinear dynamics in motor. We take the basic dynamic model from (2.14) which is the following:

$$\begin{aligned} M\ddot{q} &= D(\dot{\theta} - \dot{q}) + K(\theta - q) + \tau_{ext} \\ B\ddot{\theta} &= D(\dot{q} - \dot{\theta}) + K(q - \theta) + \tau_m - \tau_{fric} \ . \end{aligned} \tag{B.1}$$

In this differential equation, M stands for the inertia of the link and B for the inertia of the motor. The damping value D can be set to zero to change the simulation from VSEA to SEA. The spring with stiffness K is located between mass M and B. As a control input, we introduce τ_m which is the torque applied to the system by the motor. The coordinates q and θ depict the rotation of the link and the motor after gear, respectively. Friction is represented in τ_{fric}. For that, we consider the concept of *Coulomb* and *viscous friction*. Subsection B.1.1 provides more information. We don't consider gravitational forces but external torque, which is represented as τ_{ext}. Additionally to the friction, a friction observer based on the idea explained in [Tie+08] is implemented. In Figure B.2, we show the basic structure of the simulation. The *external torque*, *torque from Visco-elastic joint* and the torque due to *friction* are summed up. The *Link and Motor Dynamic* includes the equations of motions (2.15) or (2.14) and computes the rotation and its derivatives. Grouped as the *state of the system*, it serves as input for the calculations of the torques.

The simulation is a discrete system with one step offset. We run the simulation with an *ode45*-solver and a variable step size. As a maximum step size we set $1/(3\times10^3)$. As *Relative Tolerance* we chose 10^{-5}. Some controllers need higher derivatives of the coordinate of link and motor. There

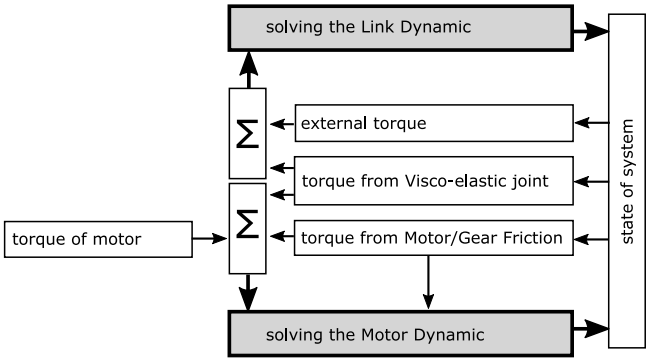

Figure B.2: The basic structure of the plant. External torque, torque of spring and damper and torque of motor/gear friction are summed up with the torque of the motor. The dynamical equation is solved in *Link Dynamic* and *Motor Dynamic*.

are several possibilities for computing them: The position signal can numerical be differentiated or – when a simulation is used – the derivatives in the solving process of the plant can be used. Using the hardware, accelerometer can provide the second derivative of the rotation. In this work, a model based estimation of the derivatives is used.

B.1.1 Identification for Friction Parameters

The easiest way to describe friction in the gear system is using the Coulomb-model. The main idea is that friction opposes motion, independent on velocity or contact area. Multiplying the Coulomb friction with the sign function leads to an opposing torque to the rotation direction. Note, that friction torque τ_{fric} is considered as a negative term in (B.1). We come to the following description:

$$\tau_{coulomb} = f_{coulomb} \cdot sgn(\dot{\theta}) \ . \tag{B.2}$$

The Coulomb factor $f_{coulomb}$ is a constant factor that describes the friction torque when the gear is rotating. As we are looking at the gear's friction which is located at motor coordinate θ, the sign function $sgn()$ indicates the direction of the gear's rotation.

The concept of viscose friction adds a velocity factor to the friction. This is caused by lubricants so that the magnitude of the friction's torque is linear proportional to the rotation. The viscous friction yields the following equation:

$$\tau_{viscous} = f_{viscous}\dot{\theta} \tag{B.3}$$

while $f_{viscous}$ depicts the viscous friction factor and $\dot{\theta}$ the rotational speed of the gear.

Table B.1: Friction in the *HarmonicDrive* Gear CPL 25-100

$\dot{\theta}_i$ [rad s^{-1}]	$\tau_{friction,i}$ [N m]
0	6.9000
0.5236	9.0000
1.0472	14.0000
2.0944	20.0000
3.6652	30.0000

This work focuses more on trends and valuation than on exact values. This is why we ignore further friction effects. These are temperature-dependent changes in lubrication and torque-dependent effects. Additionally, we do not consider the static friction which influences the break-away-torque right before the resting gear starts moving.

The model with Coulomb and viscous friction features discontinuity which may lead to problems for discrete time solvers. To avoid discontinuities caused by the sign function, a continuous function with a steep zero crossing replaces the *sgn*-function. We consider the tangens hyperbolicus function including a factor $\omega_{coulomb}$ for control the slope of the zero crossing. The parameter $f_{viscous}$ stands for the friction factor. This yields the friction model implemented in the simulation:

$$\tau_{fric} = f_{coulomb} \cdot tanh(\omega_{coulomb}\dot{\theta}) + f_{viscous}\dot{\theta} \tag{B.4}$$

The *Harmonic Drive Gear CPL 25-100* is a typical gear used in DLR robots. For this, we want to find a correlating friction model. In order to find values for $f_{coulomb}$ and $f_{viscous}$, we consider the documentation for the *HarmonicDrive* Gear CPL 25-100 in [Har16]. In there, the table *No Load Running Torque* contains the relevant values for all listed input speed. Thus, we come to table B.1. Using the method of least squares yields a linear function for given values in table B.1 to find a value for the viscous friction factor:

$$\begin{aligned}
\bar{\dot{\theta}} &= \frac{\sum_{i=1}^{n} \dot{\theta}_i}{n} \\
\bar{\tau}_{friction} &= \frac{\sum_{i=1}^{n} \tau_{friction,i}}{n} \\
f_{viscous} &= \frac{\sum_{i=1}^{n} (\dot{\theta}_i - \bar{\dot{\theta}})(\tau_{friction,i} - \bar{\tau}_{friction})}{\sum_{i=1}^{n} (\dot{\theta}_i - \bar{\dot{\theta}})^2} = 6.4042\,\mathrm{N\,m\,s\,rad^{-1}}
\end{aligned} \tag{B.5}$$

The first row in table B.1 at $\dot{\theta} = 0$ contains the Coulomb friction.

$$f_{coulomb} = 6.9\,\mathrm{N\,m} \tag{B.6}$$

Figure B.3 shows table B.1 in a plot with $\eta_{viscous}$ as linear function.

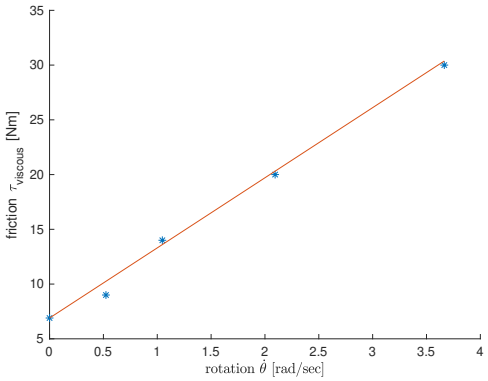

Figure B.3: Friction parameters for *Harmonic Drive gear CPL 25-100* designed with Coulomb and viscous friction model. The line shows the friction model, the stars represent the friction values from the HD documentary [Har16].

Empirical knowledge shows that the calculated friction τ_{fric} is $\approx 30\%$ lower than the friction listed in *Harmonic Drive* documentary [Har16]. As explained, this approximation is sufficient for our case.

B.1.2 Symbols and Parameters for Simulation

This work considers the definitions of the symbols that are defined in Chapter . This is useful because it reduces the number of variables and therefore the number of simulations. Nevertheless, the simulation requires specific values to run, for example for the excitation torque and the stiffness K_q. This is why we agreed on standard values for the excitation torque P_0, the spring stiffness K_q and the damper ratio ξ_q in Chapter 3.

The question hereby is the validity of the symbols in the simulation. It is already shown in Chapter 3 that the symbols are valid in the analytic system. But it is unclear, if we can use the symbols in the simulation, too. Comparing the simulation to system (2.16) or (2.20), we see that in contrast to the analytical systems the simulation contains nonlinear friction and saturation of the maximum motor torque. Thus, we expect a different outcome using the same symbols. For example, when doubling the external torque F we could reach the motor's saturation. In that case, we don't double the outcome amplitude.

To work out the influence on the symbols of explicit parameters, like K, P_0 or D_η, we run a simulation with the same symbols but with changing parameters. In this case, we change K_q from 400 $\mathrm{N\,m\,rad^{-1}}$ to 200 $\mathrm{N\,m\,rad^{-1}}$. According to Chapter , f is defined as

$$f = \frac{\omega_{\eta,n}}{\omega_{q,n}} = \sqrt{\frac{KM}{K_q B}} \,. \tag{B.7}$$

We want to maintain the value f, so we choose the corresponding value for

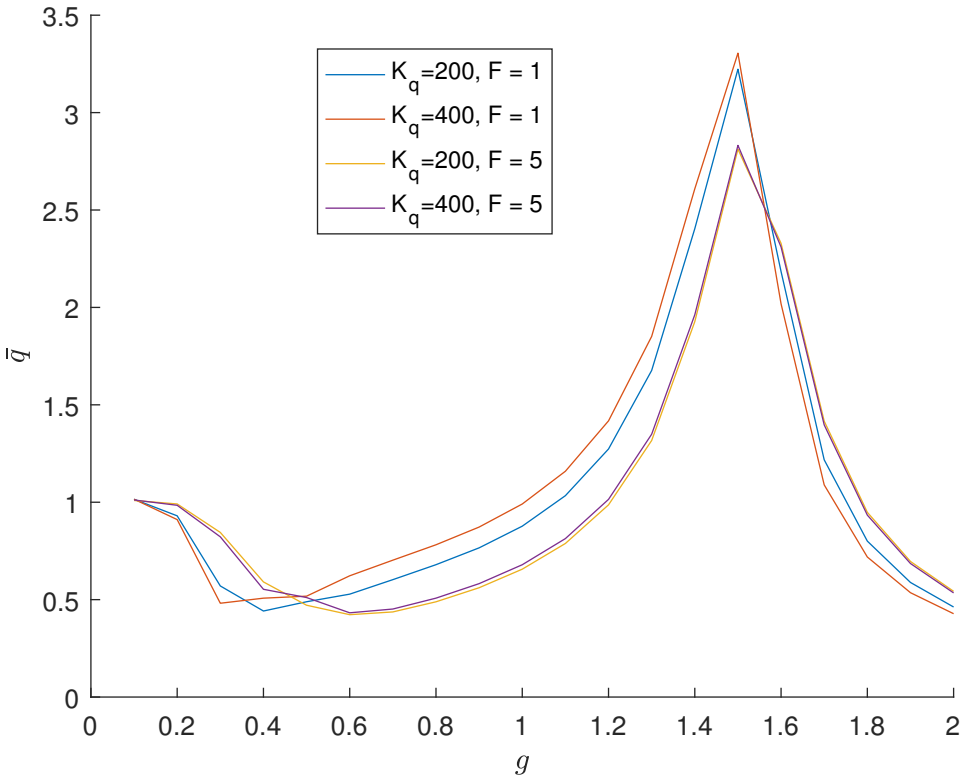

Figure B.4: In this graph, we want to illustrate the influence on dimensional parameters on the results of the simulation. We are using non dimensional parameters to reduce the number of simulations. When increasing fivefold the excitation torque, we offset this difference in the normalization of $\bar{q}$. In the simulation, we still can vary the explicit values, like P_0 and K_q, but we expect the result to be the same. This five graphs shows one set of dimensionless parameters with varying dimensional parameters.

K_q which is 337 N m rad^{-1} and 168 N m rad^{-1}, respectively. Additionally, we change the excitation torque P_0 from 1 N m to 5 N m. As we divide the resulting amplitude by the static deflection q_{stat} which is defined as P_0/K_q, we expect the amplitude to be same.

The results are depicted in Figure B.4. All graphs are similar, but slightly different. Especially when changing the excitation torque F we can see that the behavior changes to a lower maximum amplitude and a shifted minimum amplitude. Nevertheless, the similarity is sufficient for our purposes. We keep in mind that using the definitions of the symbols, we win a huge benefit in terms of reduction of complexity but simultaneous we loose accuracy.

B.2 Verification

B.3 Comparison with Analytical Closed-Loop Model

For further analysis, we want to compare the simulation results with the results of an analytic calculation. We compare link coordinate q and virtual motor coordinate η. For the simulation results, we consider the simulation as described in Chapter B. For the analytical results we consider the analytic approach presented in Subsection 3.2.1 for VESπ and 3.2.2 for ESπ controlling system.

We want to focus on two cases: In the first case, we don't consider friction. Case two is taking friction into account, based on the model explained in Section B.1. The friction is compensated with the friction observer presented in the same chapter. Additionally, we look at the two control approaches VESπ and ESπ.

The main difference between analytical closed-loop model and simulation is that the analytical model calculates the closed-loop behavior directly, while the simulation is based on the mechanical system (open-loop) (B.1) which is actuated by a controller. We expect both methods to behave in a similar manner, so we can use this method for validation.

We face the problem that the simulation and analytical approaches work with two different sets of coordinates. The simulation is based on the open-loop concept. This means, we deal with link coordinate q and motor coordinate θ only. The analytical approach processes link coordinate q and the virtual coordinate η. Therefore, the simulation output has to be transformed using equation (2.17) for the VESπ case and (2.22) for the ESπ case.

Figure B.5 shows the amplitude ratio $\bar{q}$ of link in the VESπ-system for several parameters. We overlay the analytical results with the plot of the simulation. The colored lines represent the results of the simulation while the black stars stand for the verification. Assuming that the simulation is correct, we expect the colored line and the black stars to be at the same location. For the case without friction, the simulation fits very well to the analytic solution. When considering friction, the graph indicates only a small mismatch. The simulation results match the analytical results very well. Assuming that the analytical approach is correct, the simulation works very exactly. This is an evidence that the friction observer works pretty well for coordinate q, which is link side.

However, when looking at Figure B.6, we realize that the friction observer only works well for coordinate q. This figure shows the same system but for the virtual motor amplitude η_0/q_{stat}. Here, we can see a clear difference between without and with friction. While the results match very well in the non-friction case, at the friction case it is hard to see any coherence between the two methods. The amplitudes for η_0/q_{stat} in the friction case feature a significant mismatch. This is due to the friction observer which gets its

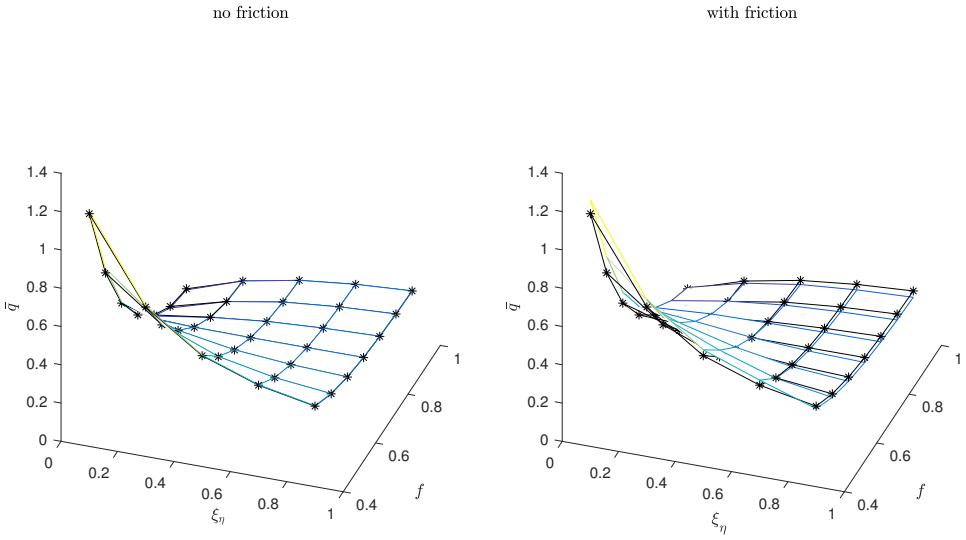

Figure B.5: Amplitude ratio $\bar{q}$ at VESπ system, without and with friction compared. The colored lines represent the results of the simulation while the black stars stand for the verification.

observation based on the link coordinate q only.

Next, we illustrate the behavior of the ESπ controller: Plot B.7 and Figure B.8 show the amplitude ratio $\bar{q}$ and $\bar{\eta}$ in the ESπ-system for several parameters. Here, we observe a similar manner. The amplitude without friction is well matched with the analytic solution, but when it comes to the η-coordinate at the friction case there is a huge mismatch.

As a conclusion, we can say that the link coordinate q matches with both, so we can assume that the simulation corresponds with the analytical equations. For the second coordinate – the virtual motor coordinate η – we observe a huge mismatch which can be explained with the restrictions of the friction observer.

Since the coordinate transformation $\theta \to \eta$ for VESπ and ESπ is dependent on the derivate of either q or θ, the friction observer has to concern both coordinate and derivate. As we can see, it is not capable of doing that. Practical experience proves that the more friction is involved (for example when excitation torque is low), the bigger is the difference between simulation result and analytic result.

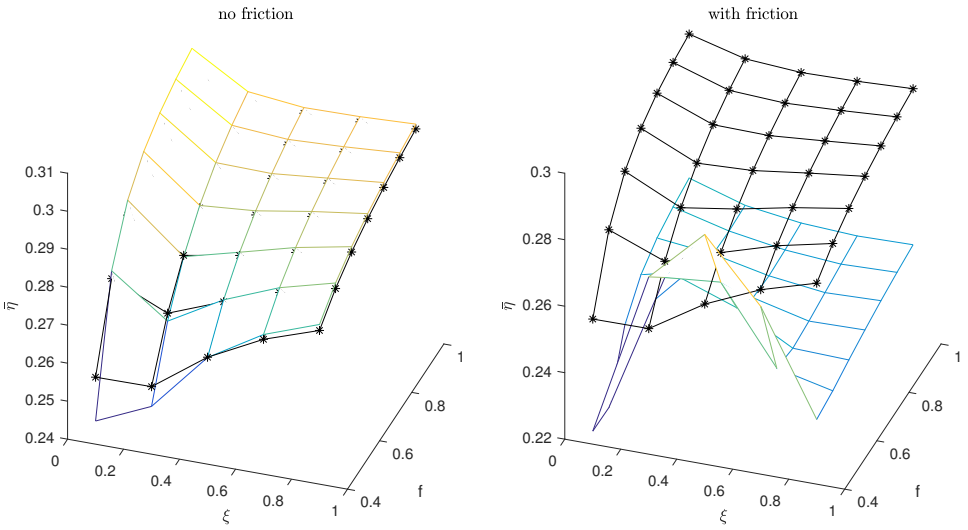

Figure B.6: Amplitude ratio of $\bar{\eta}$ at VESπ system, without and with friction compared. The colored lines represent the results of the simulation while the black stars stand for the verification.

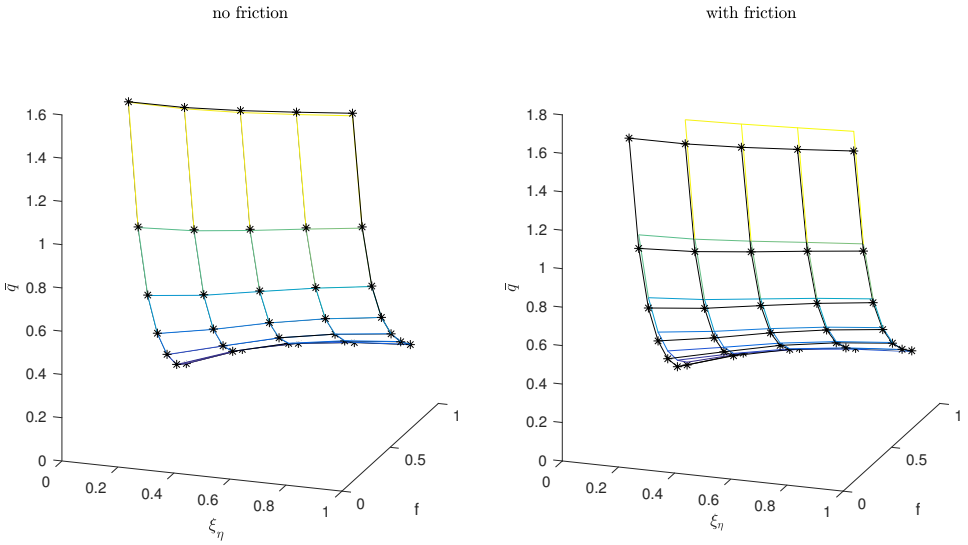

Figure B.7: Amplitude ratio $\bar{q}$ at ESπ system, without and with friction compared. The colored lines represent the results of the simulation while the black stars stand for the verification.

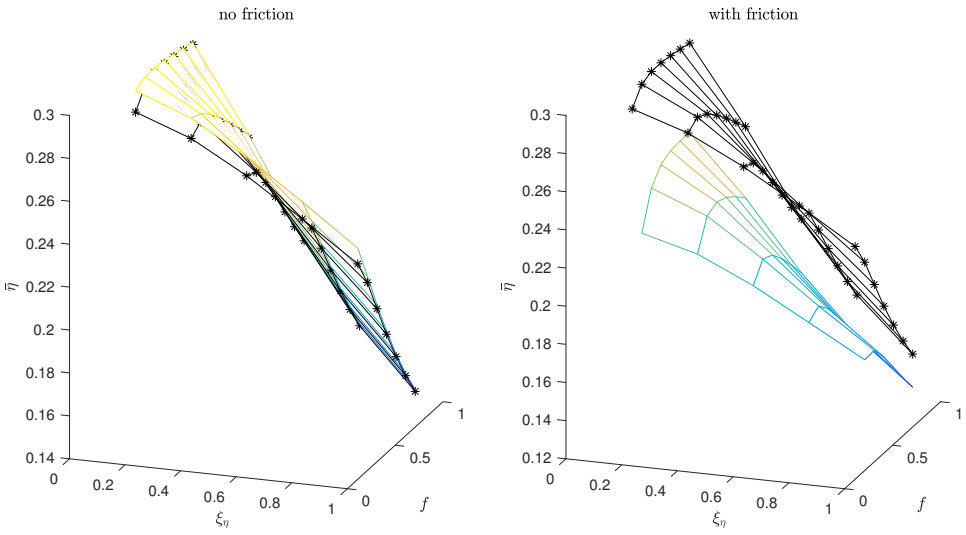

Figure B.8: Amplitude ratio $\bar{\eta}$ at ESπ system, without and with friction compared. The colored lines represent the results of the simulation while the black stars stand for the verification.

Bibliography

[Che+12] P. Cherelle et al. "The AMP-Foot 2.0: Mimicking intact ankle behavior with a powered transtibial prosthesis". In: *2012 4th IEEE RAS & EMBS International Conference on Biomedical Robotics and Biomechatronics (BioRob)* (Aug. 24, 2012). DOI: 10.1109/BioRob.2012.6290783.

[Dam+07] M. Damme et al. "Proxy-Based Sliding Mode Control of a Manipulator Actuated by Pleated Pneumatic Artificial Muscles". In: *Proceedings 2007 IEEE International Conference on Robotics and Automation* (Apr. 10, 2007). DOI: 10.1109/ROBOT.2007.364150.

[Gre+11] M. Grebenstein et al. "The DLR hand arm system". In: *2011 IEEE International Conference on Robotics and Automation* (Apr. 9, 2011). DOI: 10.1109/ICRA.2011.5980371.

[Har16] HarmonicDriveAG. *Engineering Data CPL-2A Component Set.* June 2016. URL: https://harmonicdrive.de/fileadmin/user_upload/2014_12_ED_1019655_CPL_2A.pdf.

[Har56] D. Hartog. *Mechanical Vibrations. Fourth Edition. J. P. Den Hartog. McGraw-Hill, New York, 1956. 67s. 6d.* Vol. 61. 554. Cambridge University Press (CUP), Feb. 1956, p. 139. DOI: 10.1017/s0368393100131049.

[IRS08] S. Infanti, J. Robinson, and R. Smith. "Viscous Dampers for High-Rise Buildings". In: *The 14th World Conference on Earthquake Engineering* (Oct. 12, 2008). URL: http://www.iitk.ac.in/nicee/wcee/article/14_11-0060.PDF.

[Kep+18a] M. Keppler et al. "Elastic Structure Preserving Impedance (ESpi) Control for Compliantly Actuated Robots". In: *2018 IEEE/RSJ International Conference on Intelligent Robots and Systems (IROS)* (Oct. 1, 2018).

[Kep+18b] M. Keppler et al. "Visco-Elastic Structure Preserving Impedance (VESpi) Control for Compliantly Actuated Robots". In: *ECC 2018 – European Control Conference 2018* (June 13, 2018).

[Loe+16] F. Loeffl et al. “The DLR C-runner: Concept, Design and Experiments”. In: *2016 IEEE-RAS 16th International Conference on Humanoid Robots (Humanoids)* (Nov. 15, 2016). DOI: 10.1109/HUMANOIDS.2016.7803359.

[PW95] G. Pratt and M. Williamson. “Series Elastic Actuators”. In: *Proceedings 1995 IEEE/RSJ International Conference on Intelligent Robots and Systems. Human Robot Interaction and Cooperative Robots* (Aug. 5, 1995). DOI: 10.1109/IROS.1995.525827.

[Spo87] M. Spong. “Modeling and Control of Elastic Joint Robots”. In: *Journal of Dynamic Systems, Measurement, and Control* 109.4 (1987), p. 310. DOI: 10.1115/1.3143860.

[Tie+08] L. Tien et al. “Friction observer and compensation for control of robots with joint torque measurement”. In: *2008 IEEE/RSJ International Conference on Intelligent Robots and Systems* (Sept. 22, 2008). DOI: 10.1109/IROS.2008.4651049.

[WF16] S. Wolf and J. Feenders. “Modeling and benchmarking energy efficiency of Variable Stiffness Actuators on the example of the DLR FSJ”. In: *2016 IEEE/RSJ International Conference on Intelligent Robots and Systems (IROS)* (Oct. 9, 2016). DOI: 10.1109/IROS.2016.7759104.